

Scientific Prospects for Hard X-ray Polarimetry

H. Krawczynski^{a,*}, A. Garson III^a, Q. Guo^a, M. G. Baring^b, P. Ghosh^a,
M. Beilicke^a, K. Lee^a

^a *Washington University in St. Louis, Department of Physics and McDonnell Center for the Space Sciences, 1 Brookings Dr., CB 1105, St Louis, MO 63130*

^b *Rice University, Department of Physics and Astronomy - MS 108, P. O. Box 1892, Houston, Texas 77251*

Abstract

X-ray polarimetry promises to give qualitatively new information about high-energy sources. Examples of interesting source classes are binary black hole systems, rotation and accretion powered neutron stars, Microquasars, Active Galactic Nuclei and Gamma-Ray Bursts. Furthermore, X-ray polarimetry affords the possibility for testing fundamental physics, e.g. to observe signatures of light bending in the strong gravitational field of a black hole, to detect third order Quantum Electrodynamics effects in the magnetosphere of Magnetars, and to perform sensitive tests of Lorentz Invariance. In this paper we discuss scientific drivers of hard (>10 keV) X-ray polarimetry emphasizing how observations in the hard band can complement observations at lower energies (0.1 - 10 keV). Subsequently, we describe four different technical realizations of hard X-ray polarimeters suitable for small to medium sized space borne missions, and study their performance in the signal-dominated case based on Monte Carlo simulations. We end with confronting the instrument requirements for accomplishing the science goals with the capabilities of the four polarimeters.

Keywords: Hard X-ray Polarimetry, Instrumentation, Compton Effect, X-ray detectors, Binary Black Holes, Neutron Stars, Pulsars, Gamma Ray Bursts, Active Galactic Nuclei, Blazars, Lorentz Invariance Violation

*Corresponding author.

Email address: krawcz@wuphys.wustl.edu, Tel. 314 935 8553, Fax. 314 935 6219 (H. Krawczynski)

1. Introduction

Compared to observations in other parts of the electromagnetic spectrum, X-ray observations are of particular interest for the study of mass accreting black holes and neutron stars because these objects are X-ray bright and the X-rays originate very close to the compact objects. It is thus not surprising that X-rays are key to explore the properties of these objects. Whereas several X-ray imaging, spectroscopy, and timing missions have made spectacular discoveries over the last three decades [1, 2, 3, 4, 5, 6], only one dedicated X-ray polarimetry mission has been launched so far. One of the reasons is that it is difficult to measure the polarization of an X-ray beam: whereas the arrival direction, arrival time, and energy of individual photons can be measured with extremely high accuracy, many hundreds of photons are needed to make even rough measurements of the three Stokes parameters P , Q , and V which characterize the polarization properties of an X-ray beam. The only dedicated X-ray polarimetry mission to date OSO-8 [7] detected a 2.6 keV and 5.2 keV polarization of the X-rays from the Crab Nebula of $\sim 20\%$ and a polarization angle aligned around 30 degrees oblique to the X-ray jet [8]. For Cyg X-1 weak evidence for polarization on a level of a few percent was found [9]; for other galactic compact objects upper limits on the polarization degree of a few 10 percent were measured [9, 10]. Recently, two instruments on the *INTEGRAL* satellite were used to constrain the polarization of the hard X-ray emission from the Crab Nebula. Based on the analysis of data from the SPI instrument (SPectrometer on *INTEGRAL*), Dean et al. [11] report tentative evidence for a $46\% \pm 10\%$ polarization degree of the 100 keV-1 MeV emission. The analysis of 200 keV - 1 MeV data from the IBIS instrument (Imager on Board the *INTEGRAL* Satellite) indicates an even higher polarization fraction [12]. The polarization direction seems to be aligned with the orientation of the X-ray jet at these energies [11, 12]. Models predict that galactic sources (e.g. binary black holes and neutron stars) and extragalactic sources (e.g. blazars, Gamma-Ray Bursts, GRBs) exhibit linear polarization degrees of a few percent and a few tens of percent, respectively, slightly below the sensitivity of the OSO 8 experiment. A mission with an order of magnitude improved sensitivity over OSO 8 should thus be able to detect the polarization of many objects, and to provide spectacular galactic and extragalactic results.

Recent technological progress namely photo-electron tracking gas detectors [13, 14] have opened up the possibility to design small X-ray missions

with more than two orders of magnitude better polarization sensitivities than OSO 8. The Gravity and Extreme Magnetism SMEX (*GEMS*) mission [15] with excellent polarimetry sensitivity in the 2-10 keV energy band has recently been approved as a NASA mission. *GEMS* is projected to achieve a Minimum Detectable Polarization (MDP) degree of about 3% for a mCrab source and an integration time of 1000 ksec. *GEMS* will have a single-photon energy resolution of between 15% and 20% Full Width Half Maximum (FWHM) and no imaging capabilities. At 0.5 keV *GEMS* will fly a student polarimeter with modest sensitivity.

We expect that *GEMS* will fulfill the high expectations and will motivate one or several follow-up missions. A follow-up mission may feature:

- improved sensitivity over the 2 keV - 10 keV energy range combined with an improved energy resolution,
- a broader energy bandpass with excellent sensitivity at lower (<2 keV) and/or higher (> 10 keV) energies,
- the capability to do spectroscopic imaging polarimetry enabling the acquisition of 2-D maps of extended sources with spectroscopic and polarimetric information,
- a wide field of view (FoV) polarimeter with the possibility of measuring the polarization of transient sources as for example Gamma-Ray Bursts.

In this paper, we focus on the possibility to measure the polarization of hard X-rays (>10 keV) with narrow FoV instruments and wide FoV instruments. The soft gamma-ray telescope on board of the Japanese/US *ASTRO-H* mission (launch foreseen in 2013) will be able to do some hard X-ray Compton polarimetry using a combination of a collimator, Si pad detectors and CdTe pixel detectors [16]. With an effective area of >30 cm² for Compton scattered events, the soft gamma-ray telescope on board of *ASTRO-H* should be able to verify some of the theoretical predictions discussed in this paper if on-ground and in-orbit calibration measurements can be used to reduce the systematic uncertainties below the level of the observed polarization effects.

In Section 2 we summarize the science drivers for hard X-ray polarimetric observations. In Section 3 we discuss four different experimental approaches suitable for small to mid size space missions, and present a comparative study of the performance of the different polarimeters based on Monte Carlo

simulations. In Section 4 we summarize the results of the previous sections and critically discuss which science objectives may be addressed with the experimental approaches discussed before.

The interested reader can consult [17, 18, 19] for reviews of X-ray polarimetry and for information about different X-ray polarimeters.

2. Science drivers for hard X-ray polarimetry

2.1. Binary black holes

Binary black hole (BBH) systems such as Cyg X-1 are among the brightest X-ray sources in the sky and can reach flux levels during major flares similar to the flux from the Crab Nebula (see the review by Remillard & McClintock [20]). The X-rays from a flat space Newtonian accretion disk are expected to be polarized owing to scatterings in the disk (e.g. [21, 22, 23]). Stark & Connors [24], Connors et al. [25], and Connors & Stark [26] showed that relativistic aberration and beaming, gravitational lensing, and gravitomagnetic frame-dragging result in an energy dependent polarization fraction and polarization degree. The energy dependence of the polarization properties stems from the fact that higher energy photons originate closer to the black hole and are affected more by relativistic effects than lower energy photons. Recently, Dovciak et al. [27, 28] studied the polarization of X-rays from accretion disks illuminated by a non-thermal X-ray source “above” the disk, as well as the observational consequences of different atmospheric depths. Agol & Krolik [29] and Schnittman & Krolik [30, 31] included in their calculation the effect of “returning radiation”, X-rays which leave the accretion disk, hit it again after gravity deflects them around the black hole, and are eventually scattered into direction of the observer. At energies about the thermal peak (a few keV for typical BBH systems), the returning radiation can dominate the polarization signature, causing the polarization direction to swing from a horizontal orientation at low energies (perpendicular to the rotation axis, as in the flat-space Newtonian limit discussed by Chandrasekhar) to vertical (parallel to the rotation axis) at higher energies.

Schnittman & Krolik [30, 31] studied the X-ray polarization in the thermal state and in the hard/steep power law state (for definitions see [20]). Spectropolarimetric observations of the thermal state make it possible to test models of the radius dependent emissivity of the gas in the accretion disk and the plunging region. If the X-ray emission follows a Novikov-Thorne zero-stress emissivity profile, the spectropolarimetric data can constrain the

inclination of the inner accretion disk and the mass and spin of the black hole. Observations in the hard X-ray band have to cope with relatively low >10 keV fluxes in the thermal state. However, the hard X-ray polarization degree is expected to be much higher ($>10\%$) than in the 2-10 keV energy band ($\sim 3\%$) owing to the dominance of returning radiation at high energies. Owing to the soft thermal spectrum a good sensitivity in the 10 keV - 30 keV energy range will be important for these observations as a detection at higher energies is unlikely. The hard X-ray observations are of great interest as they probe the innermost regions of the accretion flow constraining the properties of the accretion flow close to the black hole and the spin of the black hole. Multi-epoch broadband spectropolarimetric observations can pin down the disk inclination and the black hole spin. The spin and inclination remain constant over very long times, while the disk, accretion rate, and coronal properties change on days-to-months times. High signal to noise ratio observations with good energy resolution may even make it possible to search for deviations from the General Theory of Relativity.

In the hard/steep power law (hard/SPL) state a hot corona comptonizes the disk emission. Owing to the dominance of coronal emission, observations in the hard/SPL state are not suited to constrain the properties of the central accretion flow nor the spin of the black hole. However, hard X-ray observations will be key to probe the properties of the corona. Schnittman & Krolik [31] examined the spectropolarimetric signatures of various corona geometries. The emission properties depend on a large number of parameters including the BH mass and spin, the BBH inclination, the accretion rate, and the coronal properties such as its homogeneity, the vertical scale height, the temperature, the optical depth, and the covering fraction. Constraining these parameters will require multiple spectropolarimetric observations at different flux levels. Although parameter degeneracies will likely render it impossible to pin down all these parameters, the X-ray polarimetry data will allow sensitive tests of corona models and their geometry. For example, a solid prediction resulting from uniform corona models is a high degree ($>2-10\%$) of polarization at >10 keV energies. A sensitive hard X-ray polarimeter may scrutinize the BBH emission up to energies of 100 keV and above. A broad energy bandpass and a reasonable energy resolution (20% or better) are thus important for exploring BH coronas. Quasi-periodic oscillations (QPOs) are most pronounced at >6 keV energies and are thus thought to originate in the hot corona [20]. The comparison of the polarization signature with timing properties at different epochs should make it possible to

lead to constraints on the location, size, and coherence of the regions from which the QPOs originate [31].

2.2. Neutron Stars, Pulsars, Pulsar Wind Nebulae, and Magnetars

Magnetic neutron stars are expected to display a range of polarization phenomena in hard X-rays which have essential bearing on several aspects of the basic physics of radiation transfer in strongly magnetized plasmas.

Isolated pulsars provide a neutron star source class that offers exciting possibilities for polarimetric probes in the hard X-ray band. Young pulsars possess high fields, and are bright in gamma-rays, which lead to their detection with the *Fermi* Gamma-Ray Space Telescope [32]. The photons detected above 100 MeV are most likely curvature radiation or synchrotron emission from tenuous pair plasmas in the magnetospheres. This contention applies also to the hard X-ray emission in the 10 keV - 1 MeV window seen in famous pulsars like the Crab and Vela. Yet, because of pair cascading in both slot-gap (e.g. [33]) and outer gap (e.g. [34]) pictures for gamma-ray pulsar emission, hard X-ray band radiation is more likely to constitute a synchrotron signal, since its rate is very high when the pairs produced have significant pitch angles. Synchrotron and curvature emission possess similar spectral indices, whether coming from uncooled electron populations, or strongly-cooled particles. Hence another tool is needed to discriminate between the two, and polarimetry can enable such. The degree of polarization from either process is high, and in uniform fields couples to the spectral index for power-law electron distributions according to Eq. (1) below. In curved magnetospheric fields, different observational perspectives relative to the local field direction are sampled, depending on the pulse phase, and so the net polarization signal can be lowered somewhat. Pulse profiles can be used as a diagnostic of typical magnetospheric locales using the gamma-ray spectrum (e.g. [35, 36]). Yet, the orbital planes for accelerating charges that govern these two radiation processes are orthogonal to each other. Accordingly, for very confined emission regions, the Stokes vector for synchrotron emission is perpendicular to that for curvature radiation. Superposing different emission regions smears this discriminator somewhat, but the net product is distinctive polarization angle (PA; vector on the sky) “swings” during the pulse period: the curvature pulse PA profile should display a markedly different phase morphology from that for the synchrotron process. Hence, in conjunction with the light curve, measuring both the polarization degree and angle as functions of phase and energy should probe both the electron distribution

shape, the spatial extent of the emission region to some degree, and help decide which physical process is dominating the signal in different X-ray bands. Ideal neutron stars as candidates for such spectropolarimetric studies are the Crab, Vela and PSR B1509-58 pulsars, because they are all very bright in X-rays, typically 20-50 mCrab in the range 50-500 keV, and their spectral index changes from 10 keV to 1 MeV.

Neutron stars with strong magnetic fields can exhibit cyclotron features occurring at the cyclotron resonance energy $E_c \equiv \hbar\omega_c \approx 11.6B_{12}(1+z)^{-1}$ keV, where B_{12} is the magnetic field B in units of 10^{12} G, and z is the gravitational redshift at the site of resonance (e.g., at or near the surface of a neutron star). Such features have now been detected in the X-ray spectra of about fifteen accretion-powered pulsars in the energy range $\sim 15 - 50$ keV, indicating magnetic field strengths in the range $B_{12} \sim 1 - 5$ [37, 38, 39, 40]. Future hard X-ray studies may find similar features at higher energies in other pulsars, indicating higher magnetic fields. Near cyclotron resonance, oscillations in the *amount* of linear X-ray polarization with pulse phase display a pronounced maximum in their amplitude [41], which makes this energy range the optimal one for studies of such oscillations. The correlations between these oscillations in an accretion-powered pulsar and its pulse profile are one of the best known diagnostic probes of the beam shape of the pulsar. Detailed calculations have shown that for a pencil beam, oscillations in the polarization amount are expected to be *out of phase* with the pulse (i.e., maximum of polarization at pulse minimum), while for a fan beam, polarization oscillations are expected to be *in phase* with the pulse (i.e., maximum of polarization at pulse maximum) [41]. Moreover, there will be an energy-dependence to the polarization within a line feature, and this will be different between the fundamental and higher harmonics due to photon spawning. Measurements of these properties will provide diagnostics on viewing angle and effective optical depth. Thus hard X-ray polarization studies near the cyclotron resonance energies of accretion-powered pulsars have great potential for being pioneering probes into the beam shapes of these pulsars, which will constrain models of accretion flow to the magnetic poles of such pulsars. Bright accreting pulsars like 4U 0115+63 can exhibit 10 keV - 50 keV fluxes of $\sim 1/4$ Crab [37]. The particular source 4U 0115+63 is a good target as five cyclotron resonance features were observed up to energies of 50 keV. At higher energies the spectrum runs out of statistics [42].

Birefringence of the vacuum in a strong magnetic field is a prediction of fundamental physics which may be amenable to direct demonstration through

X-ray polarization studies of accretion-powered pulsars. The crucial energy in this context is that of vacuum resonance $\hbar\omega_0 \approx 13B_{12}^{-1}n_{e,22}^{1/2}$ keV, where vacuum birefringence effects cancel the plasma effects, and the *direction* of polarization is expected to rotate by 90 degrees due to *mode conversion*. Here, $n_{e,22}$ is the electron density in units of 10^{22} cm $^{-3}$. Mode conversion is a phenomenon which occurs through an interplay between (a) the photospheres corresponding to the ordinary and extraordinary modes of electromagnetic wave propagation in magnetized birefringent plasmas, and (b) the above vacuum resonance point ([43, 44] and references therein). In accretion-powered pulsars with magnetic fields in the range $10^{11} - 10^{12}$ G and at accretion rates corresponding to electron densities in the range $10^{22} - 10^{23}$ cm $^{-3}$, the vacuum resonance energy occurs in the hard X-ray band, underscoring the importance of hard X-ray polarization studies in exploring this phenomenon. Indeed, a measurement of the above rotation of polarization would be the first observational confirmation of the fundamental idea of vacuum birefringence. Bright accretion powered pulsars like Her X-1 and Cen X-3 exhibit hard X-ray fluxes on the order of 50 mCrab [45].

For magnetars, which are believed to be isolated neutron stars with super-strong magnetic fields in the range $10^{14} - 10^{15}$ G, the above ideas of vacuum resonance lead to a completely different prediction [46]. The direction of X-ray polarization in these objects is expected to remain *unchanged* as one passes through the vacuum resonance point. The vacuum resonance energy is somewhat more difficult to estimate for these objects due to uncertainties in the plasma densities at the sites of their X-ray emission, but it is clear from the above estimate that it will be in the hard X-ray / soft γ -ray band for densities $n_e \sim 10^{17} - 10^{20}$ cm $^{-3}$. A demonstration of this differential behavior in polarization rotation between known accretion-powered pulsars and suggested magnetars would be a strong indication of a different role of vacuum resonance in the latter, and so a probe of exotic phenomena in super-strong magnetic fields. Particularly suitable for such studies would be the soft gamma repeaters (SGRs). The SGR 1806-20 normally exhibits hard X-ray fluxes of 0.2 mCrab [47]. During the giant outburst of December 2004, this SGR exhibited hard X-ray fluxes on the order of the flux from the Crab Nebula. The >80 keV flux integrated over 400 sec was 2.6×10^{-4} erg cm $^{-2}$ [48].

In the lower density magnetospheres of magnetars different polarizing influences can be found. Observationally, this is probably mediated by magnetic Compton scattering in the very strong fields, which is extremely effi-

cient, more so than curvature emission or bremsstrahlung. The manifestation of Compton scattering comes in two varieties in two different wavebands. In the classical X-ray band, anomalous X-ray pulsars and soft gamma repeaters both exhibit steep X-ray power-law tails appended to the thermal peak (e.g. [49]). These have been modeled by repeated Compton scattering by mildly-relativistic electrons (e.g. [50, 51]) in collisions well below the resonance in the cross section at the cyclotron energy. The collision rates are strongly-dependent on the angle the photon momenta make to the local magnetic field, and to their polarization state. Hence, phase-dependent polarization observations of these tails below around 10 keV should probe both the locale of the emission (equatorial versus near the magnetic pole) and the observer’s viewing angle. Quiescent magnetar signals also exhibit hard X-ray tails extending up to around 150 keV [52, 53, 54]. These probably are generated by impulsive inverse Compton scattering of soft thermal X-rays by ultra-relativistic electrons in the strong magnetar fields (e.g. [55, 51]), sampling the collisional cross section at or near the cyclotron resonance. The up-scattering spectra are strongly polarized in an energy-dependent fashion [55]. Phase-dependent spectropolarimetry can confirm the postulate of the action of resonant Compton scattering in generating these hard tails, and again provide insights into the magnetospheric locale of the emission region. A number of magnetars including 4U 0142+61, RXS J1708-4009, SGR 1806-20 and SGR 0501+4516 are amenable to such polarimetric investigations with a polarimeter which can measure 10% polarization fractions for sources at the detection thresholds of *RXTE* and *INTEGRAL*. Quiescent fluxes from these sources are generally at the 5–20 mCrab level in the 20–200 keV range.

The hard X-ray tails do not extend to much higher energies, as inferred from very constraining upper limits at > 500 keV from the *COMPTEL* instrument on the Compton Gamma-Ray Observatory (e.g. [54]). The *Fermi* Large Area Telescope (LAT) can be used to derive additional constraints on the high-energy properties of the energy spectra, but so far dedicated studies have not yet been published. If the maximum energies correspond to kinematic limits in the scattering process, then turnovers in the 200-500 keV band should have characteristic energies independent of the photon polarization. However, in the strong fields not far from the magnetar surface, photon splitting $\gamma \rightarrow \gamma\gamma$ can act as an attenuation mechanism that may forge a spectral turnover at these energies. Splitting can only occur in strong magnetic fields (e.g. [56]), and is an exotic prediction of QED. Its rate is strongly dependent on the polarization of the photon, so that measurements

of quasi-exponential turnovers whose energies depend markedly on the photon polarization would be a telltale sign of the action of splitting. Detecting such a signature would be an important confirmation of a theoretical prediction, since magnetic photon splitting has not been confirmed in the laboratory. Through the dependence of the splitting rate on the angle between the photon momentum and the magnetic field line direction and the strength of the local field, phase-dependent polarimetric observations would facilitate determination of the altitude and co-latitude of the emission region. Strong flares in SGRs possess quasi-thermal spectra with effective temperatures in the 15-40 keV range. It is believed that these emanate from fireballs (e.g. [57]), whose opacity is largely controlled by magnetic Compton scattering. At such energies, photon splitting should also be active in modifying the higher frequency portion of the spectrum. Accordingly, such bright outbursts, and the even stronger giant flares from SGRs (around 8-10 orders of magnitude brighter than magnetar quiescent emission), if detected by an all-sky monitor, offer excellent opportunities to probe the radiation physics and emission region conditions in this subset of magnetars.

2.3. Active Galactic Nuclei

Active Galactic Nuclei (AGNs) emit thermally in the hard UV band with the peak of the thermal emission falling into the 30-100 eV range. At X-rays, a hard power law emission component is observed with photon indices $\Gamma = 1.5-2$ [58, 59]. The power law emission is thought to originate from the corona through the Comptonization of thermal photons by electrons of a temperature $T_c \sim 100$ keV [60]. The polarization of Comptonized disk emission was studied by Sunyaev & Titarchuk [23] and Schnittman & Krolik [31]. The coronal emission is expected to be polarized to a higher degree (typical values of $\sim 8\%$) than in the case of BBHs (typical values of $\sim 2\%$). Owing to the large number of interactions required to increase the energy of the thermally emitted disk photons from a fraction of a keV to >10 keV, photon paths parallel to the plane of the accretion disk and the corona are more common than in the case of the photons from BBH coronae. Sunyaev & Titarchuk [23] and Schnittman & Krolik [31] find that the spectropolarimetric data can be used to constrain the inclination of the AGN. In the case that the inclination of the disk is known (e.g. from the blue edge of the broad iron line [61]), the X-ray spectropolarimetric data can be used to constrain details of the coronal model such as the number of clumps and their over-density. X-ray polarimetry studies of AGNs have to cope with low fluxes: Type 1

Seyfert AGNs like NGC 4151 and NGC 5548 have X-ray fluxes on the order of 1 mCrab [62, 63]. Furthermore, the interpretation of the data may be complicated owing to a contamination of the emission by the non-thermal emission from a jet.

2.4. Jets from Active Galactic Nuclei

The highly relativistic jets (collimated outflows) from accreting supermassive black holes at the center of galaxies are sources of electromagnetic continuum radiation all the way from the radio band to the TeV gamma-ray band. Of particular interest for the test of jet formation models are blazar observations. Blazars are accreting supermassive black hole systems with one jet aligned with the line of sight. The relativistic motion of the emitting plasma amplifies the jet emission along the direction of motion and makes blazars some of the brightest extragalactic objects in the Universe. The spectral energy distribution of the continuum emission shows a low-energy peak and a high-energy peak. According to the standard paradigm a population of relativistic electrons emits the low-energy and high-energy components as synchrotron and inverse Compton emission, respectively. Magnetic fields are thought to be an important jet component. They may even dominate the jet energy density. Furthermore, the magnetic fields are dynamically important and are believed to stabilize jets on spatial scales between a few light hours and thousands of light years.

For low-energy peaked blazars (i.e. flat spectrum radio quasars) the low-energy emission component peaks at infrared/optical wavelengths, and the high-energy emission component peaks in the MeV gamma-ray regime. The X-ray to gamma-ray emission of such objects is believed to be inverse Compton emission. Multiwavelength observations of the polarization degree and polarization direction have the potential to elucidate how the hard X-rays are emitted. In the Synchrotron Self-Compton (SSC) scenario the X-rays come from inverse Compton interactions of electrons with co-spatially emitted synchrotron photons, and one expects that the X-ray polarization tracks the polarization of the synchrotron emission at longer (radio, infrared, and optical) wavelengths [64, 65, 66]. The optical emission of blazars shows high polarization degrees [67, 68] close to the theoretical expectation for a power law electron distribution with significant pitch angles (exceeding $1/\gamma$, with γ the electron Lorentz factor) in a uniform magnetic field:

$$P_s = \frac{p + 1}{p + 7/3} \quad (1)$$

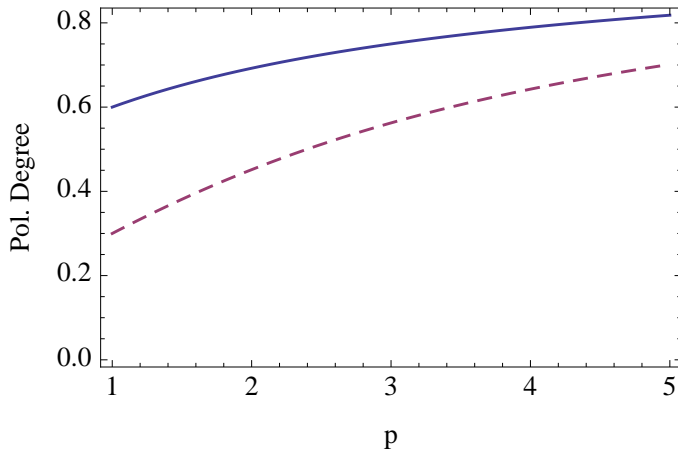


Figure 1: Polarization degree of the synchrotron emission (solid line) and the inverse Compton emission (dashed line) as function of the electron spectral index in SSC models of the continuum emission from blazars. The curves assume a uniform magnetic field, and $\sin \zeta = 1$ for the angle ζ between the magnetic field direction and the propagation direction of the SSC photons in the jet frame.

where p is the spectral index of the electron energy spectrum. Poutanen (1994) gives a simple expression for the polarization degree of the SSC emission P_{SSC} as function of P_{S} and p :

$$P_{\text{SSC}} = P_{\text{S}} \frac{(p+1)(p+3)}{p^2 + 4p + 11} \sin^2 \zeta \quad (2)$$

with ζ being the angle between the magnetic field direction and the SSC emission in the jet frame. Note that $\sin \zeta \sim 1$ is quite likely even if the angle between the jet axis and the line of sight is only a few degrees owing to relativistic aberration. Figure 1 shows the synchrotron and SSC polarization degrees as function of the electron spectral index. *GEMS* should be able to decide between the SSC scenario and alternative external Compton (EC) models in which the target photons are provided by the accretion disk, the broad line region, from an outer slow jet sheet, or from other upstream or downstream regions of the jet. Whereas the synchrotron and inverse Compton emission should show similar polarization degrees and identical polarization directions in the SSC scenario, EC models predict much lower polarization fractions ($< 5\%$) and polarization directions that depend on the seed photon source and the alignment of the jet to the line of sight [66]. High signal-

to-noise time resolved broadband spectropolarimetric observations (e.g. 0.1 keV-100 keV) would make it possible to sample the time evolution of the energy dependent flux, polarization fraction, and polarization direction of several spectral components. The observations of the polarization properties would afford the possibility to decide if different spectral components are emitted co-spatially (similar polarization degrees and directions) or not (different polarization degrees and directions). If SSC models hold, polarimetric multiwavelength observations may make it possible to identify spectral parts (e.g. in the optical and X-ray bands) which are emitted by electrons of the same population.

For high-energy peaked blazars (i.e. BL Lac objects), the low-energy emission component peaks in the X-ray band, and the high-energy emission component peaks in the GeV to TeV gamma-ray regime. In the case of “extreme synchrotron blazars” like Mrk 421, Mrk 501, and 1ES 1959+650 the low-energy synchrotron component extends from the radio band all the way to hard (~ 100 keV) X-ray band. These objects exhibit correlated X-ray and gamma-ray flares on time scales of minutes. The fast flares indicate that the X-ray/TeV gamma-ray emission originates close to the black hole where the jet energy density is highest and the jet cross section is smallest. The observations of the polarization of synchrotron X-rays might thus allow us to probe the structure of the magnetic field close to the base of the jet. Of particular interest are observations of high degrees of polarization close to the theoretical maximum indicating the presence of a uniform magnetic field. Broadband spectropolarimetric observations (e.g. 0.1 keV-100 keV) of curved energy spectra would make it possible to determine the polarization degree at different energies and for different electron spectral indices and thus to test if the polarization fraction depends on the electron spectral index as predicted by Equ. (1).

Recently, optical polarization swings by 180° in temporal coincidence with X-ray and gamma-ray flares were reported [69, 70]. If jets are threaded and accelerated by helical magnetic fields polarization swings may be produced by the field moving through a stationary shock feature [69]. If the explanation is correct it should be possible to observe such polarization swings in the soft and hard X-ray bands and to confirm the presence of a helical magnetic field structure. If the global field morphology within the jet is quite turbulent, there may be significant depolarization, and the temporal variations in the degree and angle of polarization may vary in a more chaotic manner.

For all three blazar science topics described above hard X-ray observa-

tions have one distinct advantage over soft X-ray observations: the electrons responsible for the hard X-ray emission cool faster than the electrons responsible for the soft X-ray emission. Hard X-ray observations can thus resolve time variable phenomena on shorter time scales – if the signal to noise ratio is sufficiently high. Bright blazars like Mrk 421, Mrk 501, and PKS 2155-304 can reach X-ray fluxes between 10 mCrab and 100 mCrab.

2.5. Gamma-Ray Bursts

GRBs are brief flashes of gamma-rays from random locations in the sky. For a short time period, the GRB becomes the most luminous object in the Universe. The GRB emission is thought to originate in highly relativistic jets powered by hypernovae (explosions of massive stars) [71, 72] or by coalescing neutron stars or neutron star black hole mergers (see the references in [73]). Gamma-ray opacity arguments constrain the jet bulk Lorentz factors to values $\gg 100$ [74]. The jet launching mechanism is still highly uncertain. In the case of long GRBs (>2 s) a newly formed spinning black hole inside a collapsing star may launch the jet through a combination of thermal pressure, electric fields generated by the black hole spinning in the magnetic field of the collapsing star, inertia of the stellar material, magnetic pressure, and magnetic stresses (see [75] for a comprehensive discussion). Coburn & Boggs [76] reported a strong polarization of GRB021206, however, independent analyses did not confirm the result [77]. Kalemci et al. [78], McGlynn et al. [79], Götz et al. [80] reported on *INTEGRAL* observations of GRB 041219a which were consistent with a high degree of polarization but did not support the polarization with a high statistical significance.

X-ray polarimetry has the potential to make smoking gun measurements with regards to the mechanism responsible for the prompt emission and the structure of GRB jets [81, 82, 83, 84, 85]. If the jets are threaded by uniform magnetic fields and the prompt X-ray/gamma-ray emission is synchrotron emission a GRB polarimeter would measure high polarization fractions. If GRB jets are threaded by helical magnetic fields that accelerate and confine the jets the polarization direction may exhibit a continuous swing as the helical field moves through a standing shock feature (e.g. as the jet exits the star) or as the shock moves relative to the particle accelerating shock. This would then provide a hard X-ray analog for GRBs of the polarization swing observed in the optical for the blazar 3C 279 [70].

Whereas a wide FoV hard X-ray experiment would be able to autonomously detect GRBs a narrow FoV experiment would have to rely on

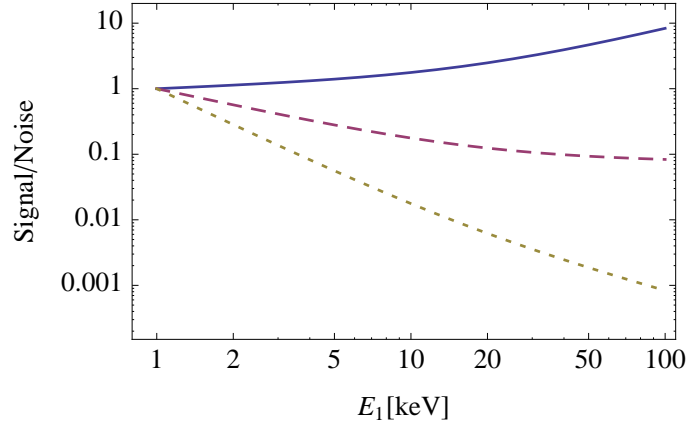


Figure 2: Signal to noise ratio (SNR) for the detection of GRBs with a wide field of view instrument as a function of the threshold energy E_1 . The SNR was computed for three different GRB photon indices ($dN/dE \propto E^{-\Gamma}$): $\Gamma = 1$ (solid line), $\Gamma = 2$ (dashed line), and $\Gamma = 3$ (dotted line). The calculations assumed a SNR limited by the noise of the diffuse cosmic X-ray background (CXB) [87] and instruments with a uniform sensitivity from $E_1 \dots E_2 = 4 E_1$. All curves were normalized to unity at $E_1 = 1$ keV.

the detection of GRBs by other experiments to perform rapid follow-up observations. The Swift BAT localizes GRBs with an accuracy of 1-4 arcmin within 20 sec after the start of the event [86]. Subsequent observations with the Swift X-Ray Telescope (XRT) improve the localization accuracy to a few arcsec a few minutes after the start of the event. The localization errors of the *Fermi* GRB detectors are of the order of a few degrees. Autonomous detection of GRBs requires a wide FoV instrument covering a substantial fraction of the sky.

In the 0.3 keV - 150 keV energy range the energy spectra of the prompt GRB emission can be described with power laws. The photon indices Γ ($dN/dE \propto E^{-\Gamma}$) vary over a wide range from ≈ 1 to ≈ 3 [88]. For a space borne mission in Low Earth Orbit the $< \sim 150$ keV background usually is dominated by the diffuse extragalactic background radiation. Figure 2 shows the signal to noise ratio as function of the threshold energy E_1 , assuming an instrument with a bandpass from E_1 to $E_2 = 4 E_1$. The graphs assume a GRB photon flux proportional to $dN/dE \propto E^{-\Gamma}$ with $\Gamma = 1, 2$ and 3, and the diffuse extragalactic background radiation model of [87]. For the hardest GRBs with $\Gamma = 1$ the signal to noise ratio improves with E_1 showing that a

large effective area and a wide energy bandpass are most important for the detection of these bursts. For softer bursts a low energy threshold is essential for a sensitive observatory.

To summarize: a GRB polarimetry mission may have a rather narrow FoV as long as other GRB missions are still operational and can distribute rapid GRB alerts. For all but the hardest GRBs a low energy threshold is crucial for detecting the GRBs. An instrument with a broad energy coverage has the obvious advantage to be able to measure the energy dependence of the polarization properties. The first catalog of GRBs detected with the Swift BAT in 2 1/2 years contains 237 GRBs with 15-150 keV fluences between 6×10^{-9} erg cm^{-2} and 4×10^{-5} erg cm^{-2} [89].

2.6. Solar and Stellar Hard X-ray Flares

Solar flares are powerful events releasing up to 10^{33} erg of which a substantial fraction goes into accelerating ions. Exceptional solar flares can accelerate ions up to energies of several 10 GeV and electrons up to energies of several 100 MeV [90]. Solar flares emit ~ 100 keV photons as Bremsstrahlung. Even though the polarization of the X-rays may be influenced by Compton scatterings of the X-rays before they leave the Sun, the hard X-ray polarization measurements have a unique potential to constrain the electron beaming and the orientation of the magnetic field loops with respect to the line of sight [91, 92, 93]. Whereas X-ray energy spectra are largely independent of the solid angle distribution of the momenta of the emitting electrons, the expected polarization degree varies from a few percent for an approximately isotropic electron distribution to 20%-25% for highly beamed distributions [94, 95, 96]. The X-ray continuum may be contaminated by thermal emission at lower (< 50 keV) energies, but above 1 MeV the gamma-ray emission mostly consists of unpolarized nuclear line emission. The best energy range for polarimetric observations is thus the window between 50 keV and 1 MeV. First tentative detections of the X-ray polarization of solar flares were reported by Bogomolov et al. [97], Boggs et al. [98], Suarez-Garcia et al. [99], Zhitnik et al. [100]. During a solar flare, the direction of the polarization vector relative to the magnetic field direction will depend on the pitch angle distribution of the emitting electrons and on the viewing angle. Firm conclusions about the direction distribution of the emitting electrons can thus require the measurement of the polarization of many solar flares and by exploring the dependence of the polarization properties on the viewing angle. The rate of solar flares depends on the solar activity. Crosby et

al. [101] report differences of the rates of solar flares of certain peak fluxes of between 1 and 2 orders of magnitude between solar cycle maximum and solar cycle minimum. Solar flares can be very bright with >20 keV peak fluxes exceeding $1000 \text{ photons cm}^{-2} \text{ s}^{-1} \text{ keV}^{-1}$ [101].

In principle, it should also be possible to detect hard X-ray flares from non-thermal electron populations from other stars. So far, hard X-ray studies of stellar flares were limited by the sensitivity of the detectors. All the hard X-ray emission recorded so far (e.g. by the BeppoSax satellite, [102]) could be explained as thermal emission [103]. Polarimetric studies of the hard X-ray emission from stars are beyond the sensitivity of the instruments discussed in this paper.

2.7. Search for Lorentz Invariance Violation

For the last two decades theoretical studies and experimental searches of Lorentz Invariance Violation (LIV) have received a lot of attention (see the reviews by [104, 105, 106, 107]). On general grounds one expects that the two fundamental theories of our time the General Theory of Relativity and the Standard Model of Particle Physics can be unified at the Planck energy scale. Under certain conditions deviations from the two theories may be observable even at much lower energies, e.g. if effects such as a tiny difference between the propagation speed of orthogonally polarized photons accumulate over cosmological distances to become measurable [108, 109].

Possible consequences of LIV are energy and helicity dependent photon propagation velocities. The energy dependence can be constrained by recording the arrival times of photons of different energies emitted by distant objects at approximately the same time [110], e.g. during a Gamma-Ray Burst [111] or a flare of an Active Galactic Nucleus [112]. The energy and helicity dependence can be constrained by measuring how the polarization direction of an X-ray beam of cosmological origin changes as function of energy [113]. Since linear polarization is a superposition of two monochromatic waves with opposite circular polarizations, a helicity dependent speed of light would lead to a rotation of the polarization direction along the photons' path. As the deviation of the speed of light from its value at low photon energies would depend on energy, the propagation through space should lead to a frequency dependent polarization swing superimposed on the source inherent variation of the polarization properties. Depending on the dispersion relations for the different photon helicities, observations over a given frequency range could lead to three different outcomes: (i) the effect could be too small to lead to

observable consequences, (ii) it could have just the right magnitude to lead to a swing of the polarization direction in the covered frequency range, and (iii) it could be so large that even observations over a narrow energy band (given by the energy resolution of the telescope) would average over several polarization swings and would lead to a zero net-polarization. The observation of a linearly polarized signal from a cosmological source can thus be used to set an upper limit on the magnitude of the LIV effect (see [114] and references therein).

If the photon velocity depends on the photon helicity, birefringence measurements tend to yield more sensitive tests of the underlying models than time dispersion measurements. If the source of the photons is at distance L and photons exhibit a group velocity difference Δv_g the measured time dispersion is

$$\Delta t \approx \frac{L\Delta v_g}{c^2} \quad (3)$$

The detection of an extremely fast ($1 \mu\text{s}$) burst of X-rays from a GRB at a light travel time of $L = 1 \text{ Gpc}$ would allow us to probe group velocity differences down to

$$\frac{\Delta v_g}{c} \approx \Delta t (L/c)^{-1} \approx 10^{-23} \frac{\Delta t}{1 \mu\text{s}} \left(\frac{L}{1 \text{ Gpc}} \right)^{-1} \quad (4)$$

The same group velocity difference would lead to a phase difference

$$\Delta\phi \approx \frac{L\nu\Delta v_g}{c^2} \quad (5)$$

where ν is the (mean) frequency of the observed photons. A measurement of the phase difference with an accuracy of $\Delta\phi = 10^\circ$ would allow us to access group velocity differences down to

$$\frac{\Delta v_g}{c} \approx \Delta\phi (L/\lambda)^{-1} \approx 10^{-37} \frac{\Delta\phi}{10^\circ} \left(\frac{E_\gamma}{100 \text{ keV}} \right)^{-1} \left(\frac{L}{1 \text{ Gpc}} \right)^{-1} \quad (6)$$

where E_γ and λ are the mean energy and wavelength of the observed photons. Comparison of Eqs. (4) and (6) demonstrates the power of polarimetric observations.

Equation (6) shows that deviations of the speed of light can be measured with an accuracy proportional to $(L/\lambda)^{-1} \propto E_\gamma^{-1}$. Measurements at higher energies and shorter wavelengths thus lead to better constraints. LIV is

thought to be a high-energy phenomenon; the deviation of the speed of light is expected to increase with energy. Using an expansion in powers of E_γ

$$\frac{\Delta v_g}{c} = \sum_{n=1}^{\infty} \eta^{(n)} (E_\gamma/E_{\text{Pl}})^n \quad (7)$$

with E_{Pl} the Planck energy, we infer that the accuracies of the birefringence constraints on the coefficients $\eta^{(n)}$ scale as $E_\gamma^{-(n+1)}$. Presently, the best constraints on the LIV coefficients come from the observations of polarized optical/UV emission from a GRB afterglow at redshift $z = 1.255$ at a frequency of 5×10^{14} Hz [114]. Polarimetric hard X-ray observations ($E_\gamma \sim 100$ keV) of a GRB or an AGN at a similar redshift would improve on these limits by 9 orders of magnitudes for $n = 1$. For $n = 2$ hard X-ray polarimetry would lead to an even larger improvement by 14 orders of magnitudes. Note that the concept of birefringence involves anisotropy. General constraints on polarization dependent LIV thus require polarimetric observations of a sample of GRBs or AGNs from different directions [115].

3. Hard X-ray polarimeters: four technical approaches and their performance

3.1. General considerations

The linear polarization of photons with energies between ~ 10 keV and several MeV can best be measured based on the Compton effect. Such measurements take advantage of the fact that linearly polarized photons are preferentially scattered into a direction perpendicular to the electric field orientation. Combining a low- Z scatterer with a high- Z absorber leads to a high probability for a Compton interaction in the low- Z material followed by a photoeffect absorption in the high- Z material. The polarization can be measured by histogramming the distribution of azimuthal scattering angles and fitting a sinusoidal modulation to the histogram. The modulation of the recorded azimuthal angles depends on the energy of the incident photons, the polar scattering angle, and the design of the detector assembly. At low photon energies the dominance of photoeffect interactions over Compton interactions results in a “low energy threshold” of a polarimeter that depends on the atomic number Z of the Compton scatterer. Figure 3 shows the “efficiency for Compton scattering” for different materials where the efficiency ϵ is defined as the ratio of the scattering cross section (including coherent

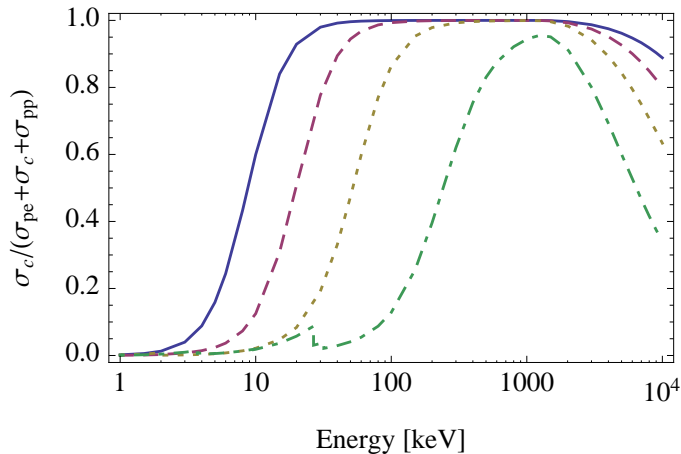


Figure 3: Compton scattering efficiency as function of energy for Li, C, Si, and CZT (from left to right). The efficiency is defined here as the Compton scattering cross section divided by the total cross section. The cross section data are from [116].

scattering) and the total cross section. If we define a threshold energy by the condition $\epsilon > 0.1$ we get threshold energies of $E_{0.1} = 4.2$ keV for Li, $E_{0.1} = 9.0$ keV for C, $E_{0.1} = 21.5$ keV for Si, and $E_{0.1} = 86.1$ keV for the semiconductor compound $\text{Cd}_{0.9}\text{Zn}_{0.1}\text{Te}$. The 50%-efficiency points are reached at the energies $E_{0.5} = 8.8$ keV for Li, $E_{0.5} = 19.8$ keV for C, $E_{0.5} = 52.1$ keV for Si, and $E_{0.5} = 246.4$ keV for $\text{Cd}_{0.9}\text{Zn}_{0.1}\text{Te}$.

The background can be reduced by requesting the temporal coincidence between a hit detected in the low-Z scatterer and in the high-Z absorber. In this case the energy threshold of the low-Z detector is likely to determine the energy threshold of the polarimeter because photons with energies of a few 10 keV ($\ll m_e c^2$) deposit only a small fraction of their energy in the first interaction. Assuming a scattering angle of 90° and neglecting the binding energy of the electron, the energy of the Compton electron as function of the energy of the primary photon E_γ is (see Fig. 4):

$$E_e = \frac{E_\gamma^2}{m_e c^2 + E_\gamma} \quad (8)$$

The Compton electron receives an energy of $E_e = 0.2$ keV, 1.2 keV, 4.5 keV, and 16 keV for $E_\gamma = 10$ keV, 25 keV, 50 keV, and 100 keV, respectively.

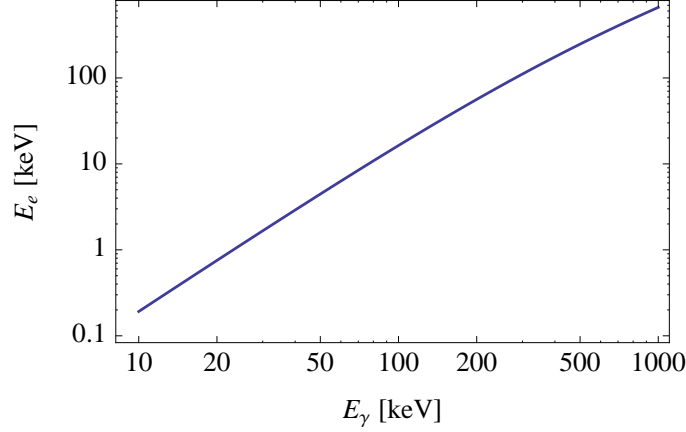


Figure 4: The energy of the Compton electron E_e as function of the energy of the primary photon E_γ for a polar scattering angle of 90° .

As mentioned above the information about the polarization of the gamma-ray beam is encoded in the azimuthal scattering angle distribution. The sensitivity of a polarimeter depends on the modulation factor

$$\mu = \frac{n_{\max} - n_{\min}}{n_{\max} + n_{\min}} \quad (9)$$

where n_{\max} and n_{\min} refer to the maximum and minimum counts in a azimuthal scattering angle histogram.

The modulation factor of Compton scattered radiation can be computed based on the Klein-Nishina cross section [117]:

$$\frac{d\sigma}{d\Omega} = \frac{r_0^2 k_1^2}{2 k_0^2} \left[\frac{k_0}{k_1} + \frac{k_1}{k_0} - 2\sin^2\theta\cos^2\eta \right] \quad (10)$$

with r_0 the classical electron radius, \mathbf{k}_0 and \mathbf{k}_1 the wave-vectors before and after scattering, θ the scattering angle (the angle between \mathbf{k}_0 and \mathbf{k}_1), and η the angle between the electric vector of the incident photon and the scattering plane. The equation for the modulation factor reads:

$$\mu(\theta) = \frac{\left(\frac{d\sigma}{d\Omega}\right)_{\eta=\pi/2} - \left(\frac{d\sigma}{d\Omega}\right)_{\eta=0}}{\left(\frac{d\sigma}{d\Omega}\right)_{\eta=\pi/2} + \left(\frac{d\sigma}{d\Omega}\right)_{\eta=0}} = \frac{\sin^2\theta}{k_0/k_1 + k_1/k_0 - \sin^2\theta} \quad (11)$$

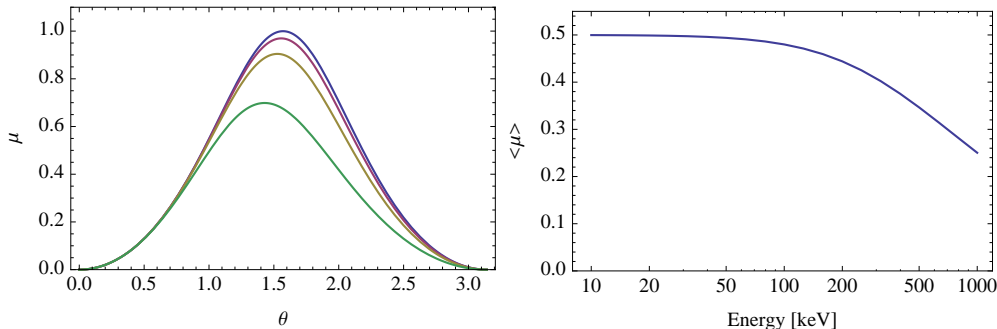


Figure 5: The left panel shows the modulation factor as function of the polar scattering angle for photon energies of 10, 100, 200, and 500 keV (from top to bottom). The right panel shows the modulation factor averaged over the solid angle and the Klein-Nishina cross section.

where k_1 can be computed as function of k_0 and θ with the help of the Compton formula:

$$\Delta\lambda = \frac{h}{m_e c} (1 - \cos\theta) \quad (12)$$

The left panel of Fig. 5 shows the modulation factor as function of θ for several initial photon energies. The right panel of the same figure shows the solid angle and cross section averaged modulation factor as function of energy. Whereas perpendicular scatterings ($\theta = \pi/2$) at low energies $E_\gamma \ll m_e c^2$ have $\mu \approx 1$, the modulation is $\ll 1$ for scatterings in the forward and in the backward direction. The modest modulation factors $\mu \sim 0.5$ achieved with the polarimeters discussed below largely result from averaging over solid angles. Systematic biases are a great concern for X-ray polarimeters. An effective means to deal with systematics is a rotation of the telescope around the optical axis. The azimuthal distribution of the detected Compton events can then be analyzed in celestial coordinates (to extract the polarization of the emission) and in detector coordinates (to estimate the systematic errors). The RHESSI experiment was rotated at 0.25 Hz, a property that was exploited for polarimetry measurements [118, 76]. The method fails for sources with substantial flux variations on the time scale of the rotation period (e.g. GRBs and fast AGN flares). Another complication are time variable backgrounds if the background changes on shorter time scales than the rotation period.

3.2. Four Detector Assemblies for Hard X-Ray Polarimetry

In this section the performance of four hard X-ray polarimeters is compared to each other. We discuss the four designs in turn. For descriptions of other hard X-ray polarimeters the interested reader might consult [17, 119, 120, 121, 19]. The first design is a detector configuration for the focal plane of a Wolter-type (imaging) mirror assembly similar to the one used in the *HERO* [122], *HEFT* [123], *InFOCUS* [125] and *NuStar* [123, 124] experiments.

The other three polarimeters are large area polarimeters which could be used with a collimator for narrow FoV observations of individual sources or with a collimator plus coded mask assembly for wide FoV imaging sky surveys.

We do not evaluate full telescope designs in this paper but limit the discussion to the detector section. We consider the particular case that the signal strongly dominates over the background and that the latter is therefore negligible. The main objective of the study is to determine how well the four designs make use of the signal photons. The design of four full experiments – including the optimization of the background shielding and the full simulation of all background sources – is outside the scope of this paper. For all four detector assemblies we assume a photon collection area of 1,600 cm². In the case of the narrow FoV polarimeter the 1,600 cm² would be the effective area of the mirror assembly (in practice: the effective area of several mirror assemblies which focus the X-rays on several identical polarimeters). For the wide FoV polarimeters the photon collection area equals the actual area covered with detectors. The estimated sensitivities correspond to the case that the detector assemblies are used with a collimator. If used with a coded mask the photon collection area is smaller than the detector area as a part ($\sim 50\%$) of the detector area is shadowed by the mask elements. The energy range of the narrow FoV polarimeter is limited at the low-energy end by the low-energy threshold of the CZT detectors (10 keV), and at the high-energy end by the high-energy cut-off of the mirror (80 keV). The energy range of the large area experiments is given at the low-energy end by the energy threshold of the scattering-detectors. The polarimeters could detect photons into the MeV energy range.

The design of the detector assembly for the narrow FoV experiment (Fig. 6, Design 1) uses a cylindrical 14 cm long 4 mm diameter scintillator rod

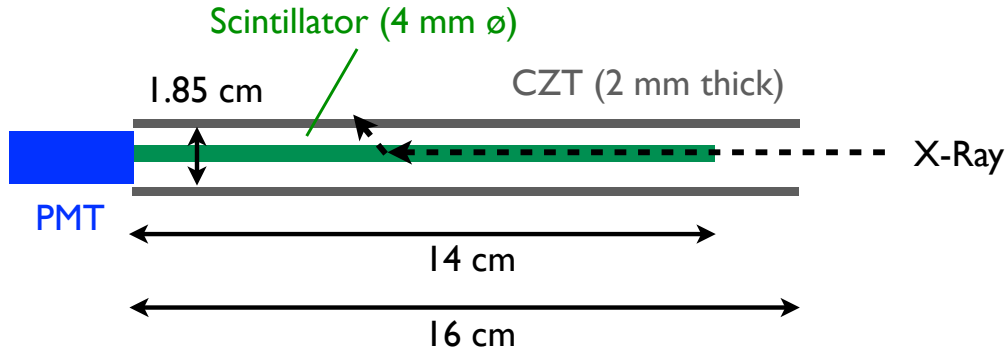


Figure 6: Design of the scintillator-CZT polarimeter (Design 1) to be used in the focal plane of a hard X-ray Wolter-type mirror assembly. The X-rays are focused on a cylindrical scintillator. The scattered X-rays are detected with pixelated CZT detectors. The scintillator (energy threshold 2 keV) can give a time coincidence signal to tag source events.

inside a rectangular 16 cm long assembly of CZT detectors. Depending on the focal length and diameter of the X-ray mirrors, larger diameter rods may be required. The major axis of the scintillator rod and the CZT detector assembly are aligned with the optical axis of a Wolter-type mirror assembly. The scintillator rod uses a fast scintillator (EJ-200¹, $\bar{Z} = 3.4$, $\rho = 1.023 \text{ g cm}^{-3}$) with a decay time of 2.1 nsec. The scintillator rod is read out with a photodetector (PMT or Geiger mode avalanche photodiode) at the rear side of the assembly. The CZT detector configuration is made of 32 detector units each $0.2 \times 2 \times 2 \text{ cm}^3$ with a monolithic cathode oriented towards the inside of the assembly and 8×8 anode pixels oriented towards the outside. We assume that the scintillator and the CZT detectors achieve energy thresholds of 2 keV and 10 keV, respectively. Two types of events are recorded: events with one or more triggering CZT pixels (high-background events), and events with a trigger of one or more CZT pixels and a trigger of the scintillator slab (low-background events). The figures below will show the results obtained for the CZT trigger. Additional results for the CZT and scintillator trigger will be described in the text. The scintillator/CZT coincidence window should exceed $\sim 1 \mu\text{s}$ – the signal formation time in the CZT detectors. The interaction depths of the energy depositions in the CZT detectors can be estimated based on the anode-to-cathode signal ratio [126, 127, 128]. The

¹<http://www.eljentechnology.com/datasheets/EJ200%20data%20sheet.pdf>

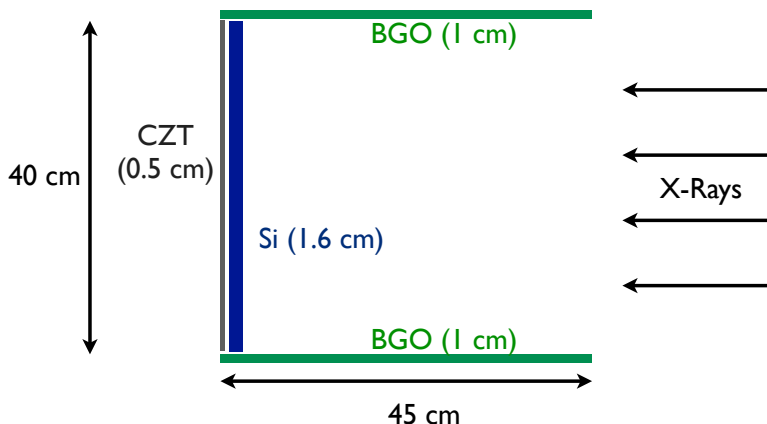


Figure 7: Design of the Si-CZT-BGO polarimeter (Design 2) to be used with a collimator or a collimator/coded mask. The assembly includes stacks of 2 mm thick Si detectors with a combined foot print of $40 \times 40 \text{ cm}^2$ and a combined thickness of 1.6 cm. Individual Si detector units are 2 mm thick, have a footprint of $10 \times 10 \text{ cm}^2$, and have crossed anode and cathode strips at a pitch of 2 mm. The Si detector assembly is followed by an array of CZT detectors (footprint: $40 \times 40 \text{ cm}^2$, thickness: 0.5 cm, each CZT detector unit: $0.5 \times 2 \times 2 \text{ cm}^3$, 64 anode pixels at a pitch of 2.5 mm, one cathode with guard ring). A ring of 1 cm thick, 5.04 cm wide and 45 cm high BGO scintillation detectors surrounds the Si and CZT detector assembly.

depth information can be used to suppress photons and charged particles that deposit their energy close to the outer edges of the CZT detector assembly. The azimuthal scattering angle is determined from the position of the pixel with the highest signal assuming that the photons scatter off the scintillator at the optical axis. As grazing angle mirror technology is limited to energies $\leq 80 \text{ keV}$, we show all results for Design 1 over the limited energy range from 10 keV to 80 keV. As will be shown below the polarimeter is very sensitive. However, it does not provide imaging information even though it is located in the focal plane of a Wolter type mirror assembly. For the description of a less sensitive polarimeter with imaging capabilities see [120].

The second detector assembly (Fig. 7, Design 2) is similar to the proposed polarimeter HX-POL [134]. The detectors cover a large area and could be used *without* focussing optics either with a pencil beam collimator or a coded mask assembly. The design uses 1.6 cm thick stacks of Si detectors in front of one layer of 0.5 cm thick CZT detectors. The Si and CZT detectors are surrounded by a 45 cm high assembly of BGO slabs (each 5.125 cm wide and 1 cm thick). The Si detector assembly is made of 4×4 detector stacks.

Each stack is made of eight Si cross-strip detectors. Each Si detector has a 10×10 cm² footprint and is 2 mm thick. The Si detectors are read out with anode and cathode strips at a pitch of 1.4 mm, with the cathode strip direction oriented 90 degrees to that of the anode strips. A particle interaction produces a charge pulse on the contacts above and below the interaction, giving the x-y position of the event. The CZT detector array is located 1 cm below the Si detector assembly and is made of 10×10 CZT detectors, each 5 mm thick and with a footprint of 4×4 cm². The CZT detectors are read out with 16×16 anode pixels at a pitch of 2.5 mm and with four quadratic 2×2 cm² cathode segments. In the case of HX-POL Application Specific Integrated Circuits (ASICs) are used to read out the Si and CZT detectors. Currently, the energy threshold of the Si and CZT detectors are 12 and 25 keV, respectively [134]. Modifications of the ASICs are expected to lead to lower energy thresholds of 5 keV and 10 keV, respectively. Each BGO slab would be read out with one photomultiplier tube and we assume an energy threshold of 30 keV. In the discussion below we distinguish between four types of events: (i) events which trigger one or more Si detectors and one or more CZT detectors, (ii) events which trigger ≥ 2 Si detectors, (iii) events which trigger ≥ 2 CZT pixels (excluding events with hits in two horizontal or vertical next-neighbor-pixels), and (iv) events which trigger one Si detector or one CZT pixel and one or more BGO detectors. If a detector component detects two energy depositions but only one interaction is needed for the reconstruction of the azimuthal scattering angle, we use the location of the higher energy deposition in the analysis. An optimized analysis which uses a “sequencing algorithm” to identify the most relevant interactions (e.g. [130]) and weighs events according to their information content is outside the scope of this paper. We note that using sequencing algorithms will only lead to a modest improvement of the sensitivity of the polarimeter. The MDP scales roughly proportional to the inverse of the square root of the number of properly reconstructed events. The fraction f of events which could potentially benefit from a more sophisticated analysis (events with more than two interactions) is less than half of all events: 38%, 28%, 13%, and 5%, for the event types (i)-(iv), respectively. The reduction of the MDP achieved with a sequencing algorithm is expected to be smaller than by a factor of $\sqrt{1+f}$, as even sophisticated sequencing algorithms cannot determine the relative order of the interactions with absolute certainty. For example, Xu et al. (2006) [130] discuss sequencing algorithms for multiple interactions in CZT detectors. For events with two detected interactions, their algorithm

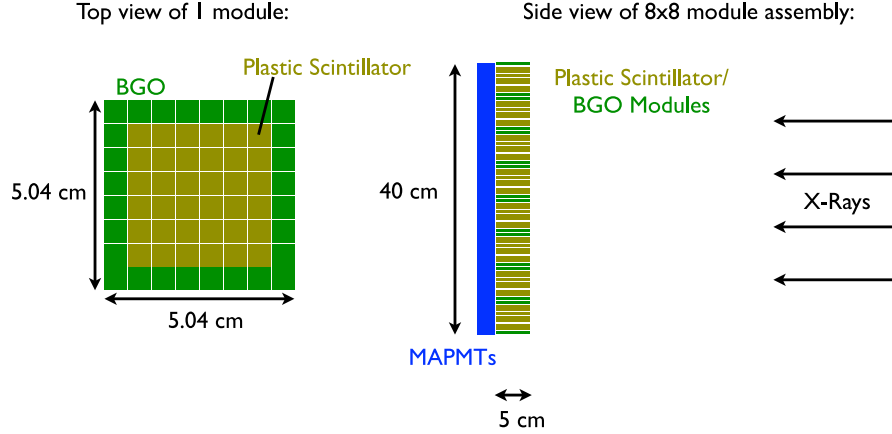


Figure 8: Design of the plastic scintillator - BGO polarimeter (Design 3) to be used with a collimator or a collimator/coded mask. The detector assembly is made of 8×8 polarimeter modules. Each module (left panel) is made of 8×8 scintillator slabs optically coupled to one 64 channel Multi Anode Photomultiplier (MAPMT). Each slab has a footprint of $0.5 \times 0.5 \text{ cm}^2$ and is 5 cm long. The inner 36 slabs are made of low-Z plastic scintillator and the outer 28 slabs are made of high-Z BGO scintillator. The right panel shows how the polarimeters modules are exposed to the incoming X-ray radiation.

identifies the first interaction with a probability of 95% at 100 keV, 80% at 250 keV, and 60% at 500 keV. For 662 keV primary photons, the algorithm identifies the correct order of the interaction for less than half of the events. Sequencing algorithm are thus expected to lead to a $\ll 20\%$ reduction of the MDP.

The third detector assembly is similar to the one proposed for the POET and GRAPE experiments [131, 132]. The detector assembly is made of an 8×8 array of polarimeter modules (Fig. 8, Design 3). Each module consists of an 8×8 array of scintillator slabs ($5 \times 5 \times 50 \text{ mm}^3$) which form a module with $5.08 \times 5.08 \text{ cm}^2$ footprint (including gaps between the scintillator slabs). Each module is read out by one Multi-Anode Photomultiplier (MAPMT) with 64 pixels. The 36 central elements of a module are low-Z plastic scintillator slabs (EJ-204). These “scattering” elements are surrounded by a “ring” of 28 high-Z BGO scintillator elements. A valid polarimetry event has one hit in the plastic scintillator and one in the BGO scintillator. Motivated by the experimental results of Bloser et al. [133] we use energy thresholds of 6 keV and 30 keV for the plastic and BGO scintillators, respectively.

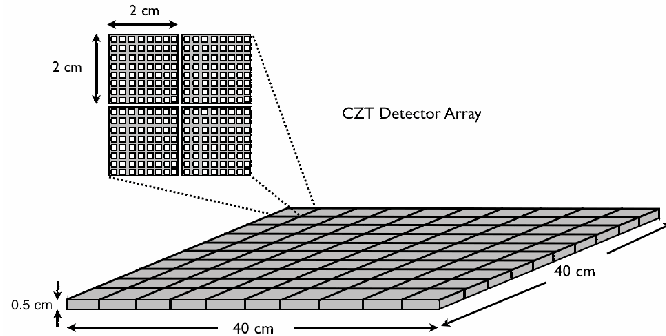


Figure 9: Design of the CZT polarimeter (Design 4) to be used with a collimator or a collimator/coded mask. The detector assembly is made of an $40 \times 40 \text{ cm}^2$ array of 0.5 cm thick CZT detectors (each CZT detector unit: $0.5 \times 2 \times 2 \text{ cm}^3$, 1024 pixels at 0.6 mm pitch, one cathode with guard ring).

The fourth detector assembly is similar to the detector assembly of the Energetic X-ray Imaging Space Telescope *EXIST*² [135] – but smaller. *EXIST* is a proposed hard X-ray all sky survey mission with a detector area of 4.5 m^2 and a tungsten shadow mask for coded mask imaging. We consider here an assembly with a detection area of $1,600 \text{ cm}^2$ made of 0.5 cm thick CZT detector units with a footprint of $2 \times 2 \text{ cm}^2$ each (Fig. 9, Design 4). We assume that the CZT detectors are read out with pixels at a pitch of 600 microns as planned for *EXIST*. The *EXIST* design foresees to bump-bond 1024 channel ASICs directly to the CZT substrates. The CZT detectors are then tiled without gaps between adjacent detectors. In the case of *EXIST*, the detectors view the sky through a hybrid coded imaging mask made of tungsten elements of 0.3 mm and 3 mm thickness, and use a partially active and partially passive shield and collimator assembly.

An assembly of CZT detectors can be used as a Compton polarimeter by analyzing events with energy depositions in two or more pixels of one or more CZT detector units. One property of CZT detectors is that energy depositions below two adjacent pixels will lead to charge induced on the two pixels (see e.g. [136]). Such “charge sharing events” can mimic Compton

²<http://exist.gsfc.nasa.gov/>

events. We find that the exclusion of events with the maximum energy depositions in horizontally or vertically adjacent pixels effectively suppresses such charge sharing events [129]. Another concern is the effect of “weighting potential cross talk” created by holes that induce charge on several adjacent pixels when drifting to the cathode side of the detector [138]. Using an ASIC with drift time measurement capability makes it possible to measure the photon interaction depth, and to properly identify true Compton events [139, 140, 138]. In practice, a CZT-only polarimeter may require such ASICs (presently not foreseen for *EXIST*). In our simulations, we assume that weighting potential cross talk leads to a negligible number of events which mimic Compton events. Following Hong et al. [137], we estimate that a single-pixel energy threshold of 5 keV can be achieved. The Harvard group (Grindlay et al.) is presently testing first 5 mm thick CZT detectors bonded to 1024 channel ASICs. We plan to make a joint study to experimentally verify the polarization measurement capabilities of the detectors.

3.3. Monte Carlo Simulations and Analysis Methods

We studied the performance of the four detector assemblies based on a Monte Carlo study with the GEANT4 package [141]. We did the simulations for Design 1 twice, once with the Standard Electromagnetic Physics List, and, once with the Livermore Low-Energy Electromagnetic Models³. In the following, we will show the results for Design 1 from the latter package as it includes a more detailed modeling of low-energy processes for photon energies down to 0.25 keV. We compared the results obtained with both simulation packages. The two packages gave slightly different rates of detected Compton events and slightly different modulation factors. The overall MDPs computed with the two packages were the same up to two significant digits. For Designs 2-4 we only did the simulations with the Standard Electromagnetic Physics List.

For each detector configuration, 2 million polarized and 2 million unpolarized photons were simulated. Photons with energies between 10 keV and 80 keV (Design 1) and 30 keV and 1 MeV (Designs 2-4) were generated according to the Crab spectrum measured with the Swift Burst Alert Telescope

³<https://twiki.cern.ch/twiki/bin/view/Geant4/LoweMigratedLivermore>

(BAT) telescope [142]:

$$\frac{dN}{dE} = 10.17 \left(\frac{E}{1 \text{ keV}} \right)^{-2.15} \text{ ph cm}^{-2} \text{ s}^{-1} \text{ keV}^{-1}. \quad (13)$$

The corresponding >10 keV energy flux is $5 \times 10^{-8} \text{ erg cm}^{-2} \text{ s}^{-1}$. The incident photons and their secondaries are tracked through the detector volumes while energy deposits, the interaction locations, and interaction processes are recorded. For all simulations the instruments were placed in a near-vacuum, similar to a low-Earth orbit environment. The GEANT4 simulation is followed by a simple detector response simulation. For each event the code computes the energy deposited in the individual detectors and - if applicable - in the pixels, strips or slabs of the detectors. A detector signal is used for the analysis if the deposited energy exceeds the energy threshold of the detector. If an event triggers more than two detector elements, only the two signals with the highest energy depositions are used. The events were re-weighted so that the number of detected photons corresponds to a 100 ksec observation of the Crab Nebula. The exposure corresponds to a >10 keV fluence of $5 \times 10^{-3} \text{ erg cm}^{-2}$.

We characterize the sensitivity of the polarimeters with the minimum detectable polarization (MDP) that can be detected on the 99% confidence level:

$$\text{MDP} = \frac{4.29}{\mu R_{\text{src}}} \sqrt{\frac{R_{\text{src}} + R_{\text{bg}}}{T}} \quad (14)$$

where μ is the modulation factor (compare Equ. 9), R_{src} is the total source counting rate, R_{bg} is the total background counting rate, and T is the integration time. The MDP has a value between 0 and 1 and gives the polarized fraction of a signal which leads to a detection on the 99% confidence level. As mentioned above, the modeling of the background, shielding, and background suppression is outside the scope of this paper. We limit our analysis to situations where the signal dominates strongly over the background ($R_{\text{src}} \gg R_{\text{bg}}$) and we assume $R_{\text{bg}} = 0$ in the following.

For some of the detector configurations discussed in the following the ϕ -distributions show modulations even for unpolarized X-ray beams because of a non-uniform detector acceptance or because of binning effects (compare Fig. 12). Following Lei et al. [17] we correct the ϕ -distributions by normalizing the polarized ϕ -histograms to the unpolarized histograms. The number of entries n_i in the i^{th} bin of the ϕ -histogram of the polarized signal is scaled

according to the equation:

$$n'_i = n_i \frac{\bar{m}}{m_i} \quad (15)$$

where \bar{m} is the mean number of entries per bin of the ϕ -histogram of the unpolarized signal and m_i is the number of entries in the i^{th} bin of this histogram. The prescription flattens the ϕ -distribution of unpolarized beams and leads to a sinusoidal modulation pattern for polarized beams.

We performed a series of simulations to study the effect of the non-uniform detector responses and binning effects of the Designs 1-4 (see Fig. 12) on the validity of Equ. (14). Non-uniformities can deteriorate the MDP of a polarimeter for given source and background detection rates, as certain ϕ -ranges may be underexposed. The relatively large fluctuations in these ϕ -ranges can lead to relatively large chance polarization degrees. As a consequence, the minimum polarization degree that can be detected with high statistical significance can increase. For each design, we used the simulated ϕ -histogram for an unpolarized incident photon beam as a template to simulate 100,000 statistically independent realizations of the histogram for one determination of the MDP. Each simulated ϕ -histogram (bin content and bin error) was corrected for the non-uniform detector response according to Equ. (15). Taking into account the proper error bars, the rescaled histogram was then fitted with the model

$$n(a_0, \phi_0; \phi) = \bar{n} (1 + a_0 \mu \cos [2(\phi - \phi_0)]) \quad (16)$$

The value \bar{n} is the mean number of entries in each bin of the histogram: $\bar{n} = n_0/N$, if n_0 events were recorded and the histogram has N bins. The values a_0 and ϕ_0 denote the best-fit polarization degree and polarization direction, respectively. After histogramming for all 100,000 artificial ϕ -histograms the best-fit a_0 -values, the MDP was determined as the a_0 -value being larger than 99% of the histogrammed values. For all four detector designs such simulations were performed for the n_0 -values of 1000, 2000, 5000, 10,000, and 20,000. For Designs 1-3 we find an excellent agreement of the MDPs from Equ. (14) with the MDPs determined from the simulations within the accuracy of the simulations ($\pm 1\%$ fractional accuracy). For Design 4 we find that Equ. (14) underestimates the MDP by a factor of 1.08 – independent of n_0 . In the discussion below, we thus use Equ. (14) for Designs 1-3. For Design 3, we multiply the result of Equ. (14) by the correction factor 1.08.

The performance estimates discussed in the following rely on Monte Carlo simulations with the GEANT4 package. The authors of the GEANT4 code

	Design 1	Design 2	Design 3	Design 4
R_{src} [Hz]	431.1	54.0	20.6	2.0
Peak efficiency	0.85 (70 keV)	0.3 (145 keV)	0.11 (145 keV)	0.035 (416 keV)
μ	0.52	0.38	0.41	0.61
MDP	0.13%	0.48%	0.73%	1.7%

Table 1: Performance of the four detector assemblies: the rate of Compton events for a Crab-like source R_{src} , the peak detection efficiency and the energy at which this efficiency is achieved, the modulation factor μ and the minimum detectable polarization MDP.

tested the simulations of Compton processes by comparing simulated results to analytical results [145]. Although the results (i.e. the scattering rates and the observed modulation factors) are consistent with simple estimates based on Eqs. (10) and (11), it would be desirable to validate the simulations by a comparison to experimental data. A comparative study of GEANT4 with the experimentally validated simulation package GEANT3 (including the GLECS and GLEPS extensions) [146, 147, 148, 149, 133] is underway (M. McConnell, private communication). As described further below, we will compare the simulations of Design 1 to experimental data in the near future.

3.4. Results

In this section we discuss the performance achieved with the four polarimeters. The most important results are summarized in Table 1. Fig. 10 shows the detection rates of the four experiments for a strong source with a Crab-like flux. Design 1 (the scintillator-CZT assembly in the focal plane of focussing X-ray mirrors) achieves the lowest energy thresholds. If the only trigger condition is a >10 keV hit in one or more CZT detectors the assembly is sensitive down to primary photon energies of 10 keV. Requiring in addition an energy deposition of >2 keV in the scintillator rod raises the energy threshold of detected photons to ~ 20 keV and the peak of the differential detection rate increases from 20 keV to 40 keV. Design 2 (the Si-CZT-BGO detector assembly) has an energy threshold of approximately 50 keV. In this case the energy threshold is determined by the energy threshold of the Compton scatterer. The threshold of the Si-Si events and the Si-BGO events is lower than for Si-CZT events owing to “back-scattered” photons which leave a larger fraction of their energy in the Si-detectors than

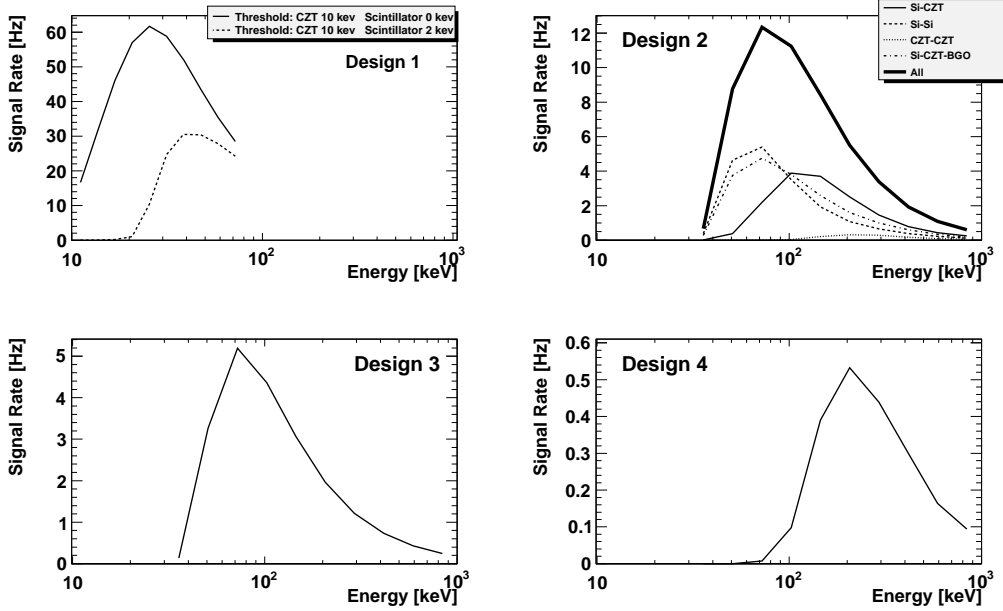


Figure 10: Differential detection rates of Compton events for the four detector designs. The figure assumes a source with a Crab-like spectrum and flux. For Design 1 the solid line shows the rate of events triggering one or more CZT detectors and the dashed line shows the rate of events triggering one or more CZT detectors and the scintillator. The latter events will be less contaminated by background. For Design 2 the solid line shows the total rate of detected Compton events; the other lines show the rates for the different types of events separately.

the “forward-scattered” photons that are subsequently photo-absorbed in the CZT detectors. Whereas Design 3 (the plastic/BGO scintillator detector assembly) also achieves a 50 keV energy threshold, Design 4 (the CZT-only experiment) has a much higher energy threshold of 100 keV owing to the dominance of photoeffect interactions over Compton scatterings at lower energies. The integral detection rates for Designs 1-4 are 431.1, 54.0, 20.6, and 2.0 Hz, respectively (Table 1).

The detection efficiencies of the four detector configurations are shown in Fig. 11 and the peak efficiencies are listed in Table 1. The efficiency is defined here as the fraction of photons impinging on a detector assembly that triggers the instrument and enters the polarization analysis. Design 1 achieves

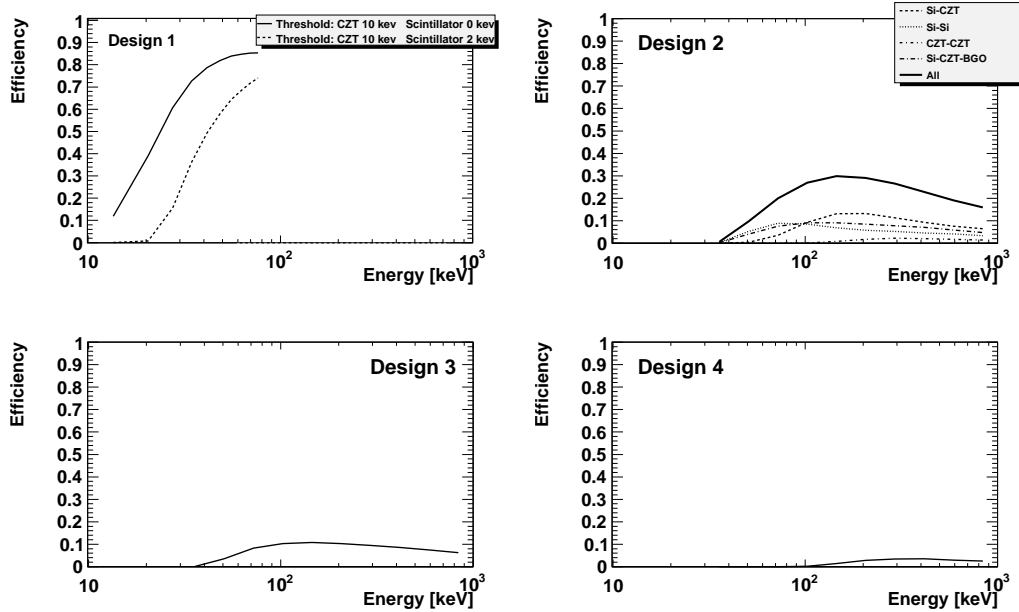


Figure 11: Differential efficiencies for the four detector assemblies. The efficiency is defined here as the fraction of all photons hitting the detector assembly which causes a trigger and enters the polarization analysis. The different lines show the results for different types of events as in Fig. 10.

high peak detection efficiencies of 85% at 70 keV. All source photons hit the scintillator rod at approximately the same location. Owing to the length of the rod a large fraction of the photons Compton scatter in the low- Z material. The small-diameter of the rod makes it possible that a large fraction of the scattered photons escape. Finally, the large solid angle coverage of the high- Z CZT detector assembly assures that a large fraction of scattered photons is photo-absorbed. The net detection efficiency of Design 2 is lower than for Design 1 and reaches a peak-value close to 30% at 145 keV. The efficiency peaks at higher energies owing to the higher Z and the higher trigger threshold of the Si Compton scatterer. The peak efficiency results from the conspiracy of several facts including the partial transparency of the Si detectors and the CZT detectors at >100 keV energies and a rather high probability that photons backscatter from the Si and escape absorption in the CZT and BGO. The peak detection efficiency of Design 3 is about 11% at 145 keV. In this detector configuration events are lost owing to the facts that

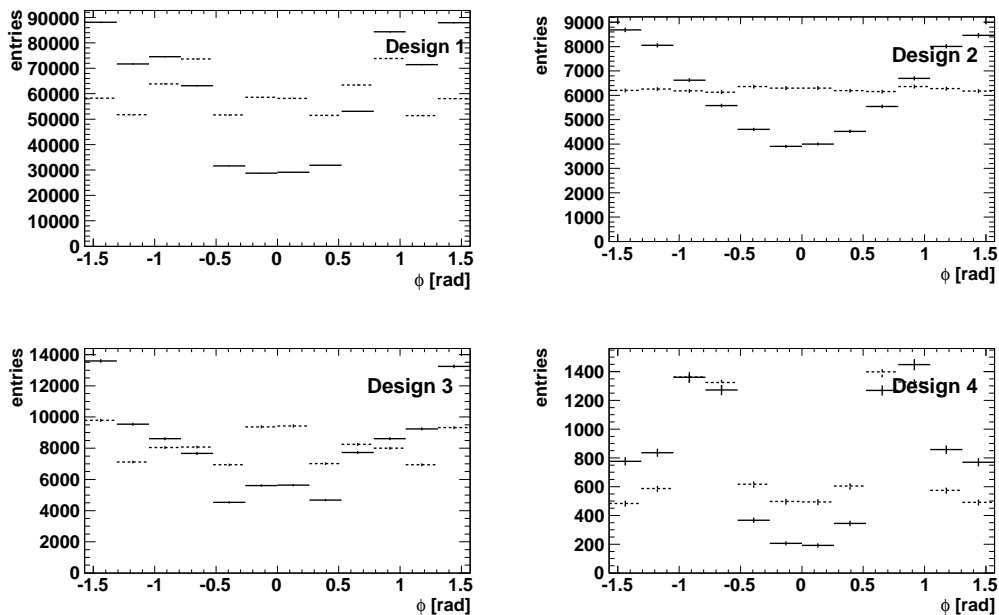


Figure 12: Distribution of azimuthal scattering angles for the four detector assemblies for polarized (solid lines) and unpolarized (dashed lines) incident beams. For Design 1 we used events which triggered one or more CZT detectors. For Design 2 the distribution is shown for events with one interaction in a Si detector and one or more interactions in a CZT detector.

(i) the low-Z plastic scintillator covers only 56% of the area and 44% of the events hit the high-Z BGO scintillator first, (ii) Compton scattered photons may be absorbed in the low-Z plastic scintillator before reaching the high-Z BGO scintillator, (iii) events can escape towards the front and rear sides of the assembly. The detection efficiency of Design 4 maxes out at relatively low values of 3.5% at 416 keV. At the low-energy end the low efficiencies result from the dominance of photoeffect interactions. Even if a photon Compton scatters it is quite likely that it is absorbed before it can propagate to the next admitted pixel. At higher energies the CZT detectors become partially transparent, and a large fraction of photons escapes the detectors towards the front or the rear of the assembly.

Figure 12 shows exemplary azimuthal scattering distributions for the four detector configurations for unpolarized and polarized X-ray beams (before

correction for non-uniformities). Here and below the graphs of Design 1 show the results for events triggering one or more CZT detectors (no scintillator trigger required); for Design 2 the results are shown for all event types.

The ϕ -distribution for an unpolarized beam shows some modulation (17%) for Design 1 owing to the large pixel size (2.5 mm) and associated binning effects. We confirmed that the binning effects go away for finer pixelated detectors by simulating Design 1 also with CZT detectors with pixel pitches of 350 microns and 600 microns. The analysis of the simulation results confirmed that the achieved MDP does not depend on the pixel pitch. For Design 2 the unpolarized ϕ -distribution for the Si-CZT events (upper right panel) is rather uniform. The unpolarized ϕ -distributions for the Si-Si events, Si-BGO events and CZT-BGO events (not shown) are also flat. An exception is the unpolarized ϕ -distribution of the CZT-CZT events (not shown, see the panel of Design 4 for a similarly modulated ϕ -distribution). The pronounced modulation (16%) of the unpolarized ϕ -distribution of Design 3 (lower left panel) results from the geometry of the detector configuration, i.e. the fact that events scattered in the plastic scintillators encounter low-Z and high-Z material with effective thicknesses that depend on the azimuthal scattering angle. A random distribution of low-Z and high-Z scattering elements in the detector plane may remove these non-uniformities. The rather large modulation (40%) of the unpolarized ϕ -histogram of Design 4 results from the limited propagation length of scattered photons in the CZT material. The histogram clearly shows event accumulations at $\phi = \pm\frac{1}{4}\pi$ corresponding to hits in diagonal next-neighbor pixels.

The correction discussed in Section 3.3 flattens the ϕ -distributions of the unpolarized beams and leads to a sinusoidal modulation of the ϕ -distributions of the polarized beams (Fig. 13). After the correction, the modulation factors are typically ~ 0.5 (see Table 1). Detector configurations for which the polar scattering angles close to $\pi/2$ are more common (e.g. in the case of the CZT-only polarimeter) achieve higher μ -values. The modulation factors exhibit only a weak energy dependence (Fig. 14).

In the following we present the sensitivities of the four polarimeters for a 100 ksec observation of a source with a Crab-like flux and energy spectrum. The integral MDPs achieved with the four detector configurations are compiled in Table 1. It should be noted that the MDPs are only valid for the case that the signal strongly dominates over the background. Design 1 achieves the lowest MDP (0.13%) followed by Design 2 (0.48%), Design 3 (0.73%),

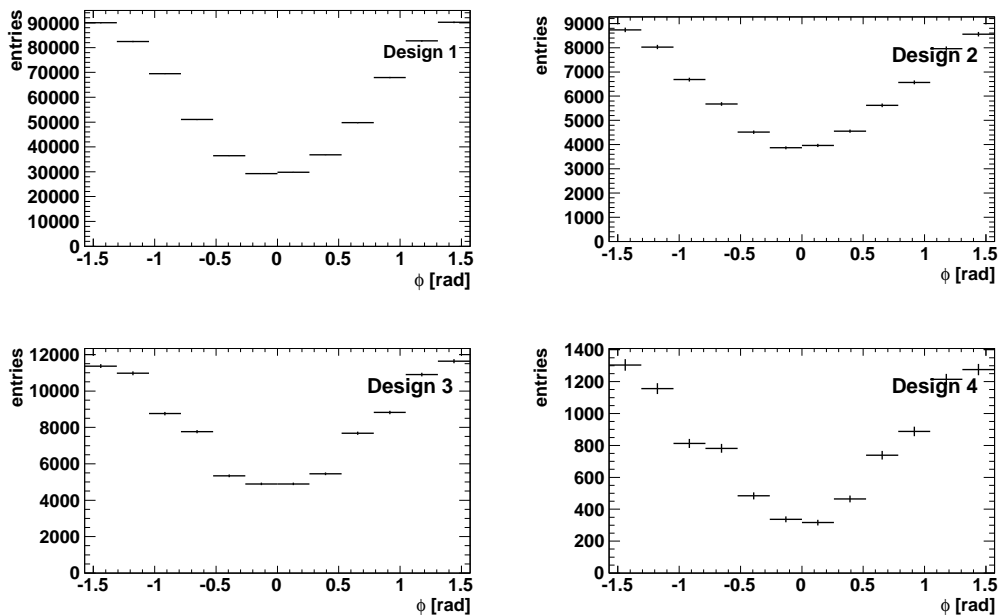


Figure 13: The distributions of azimuthal scattering angles for a polarized X-ray beam after correcting for instrumental non-uniformities for the four detector assemblies. The distributions for unpolarized beams are not shown as they are constant owing to the correction.

and Design 4 (1.7%). The energy resolved MDPs are shown in Fig. 15. One clearly sees that Design 1 is a low-energy instrument achieving the lowest MDP values at 24 keV. Designs 2 and 3 are most sensitive at ~ 70 keV, and Design 4 at 200 keV.

If Design 1 is used with the requirement of a CZT energy deposition exceeding 10 keV and a scintillator energy deposition exceeding 2 keV the detection rates drops from 431 Hz to 149 Hz and the MDP increases from 0.13% to 0.20%.

The background is expected to be lowest for the scintillator-CZT detector assembly (Design 1) in the focal plane of a Wolter-type mirror assembly: the narrow-FoV makes it possible to shield the detector assembly with a solid angle coverage close to 4π . Furthermore, the total mass of the detectors is much smaller than for the other three designs as the photon collection area is provided by the mirror assembly and not by the detectors themselves. The

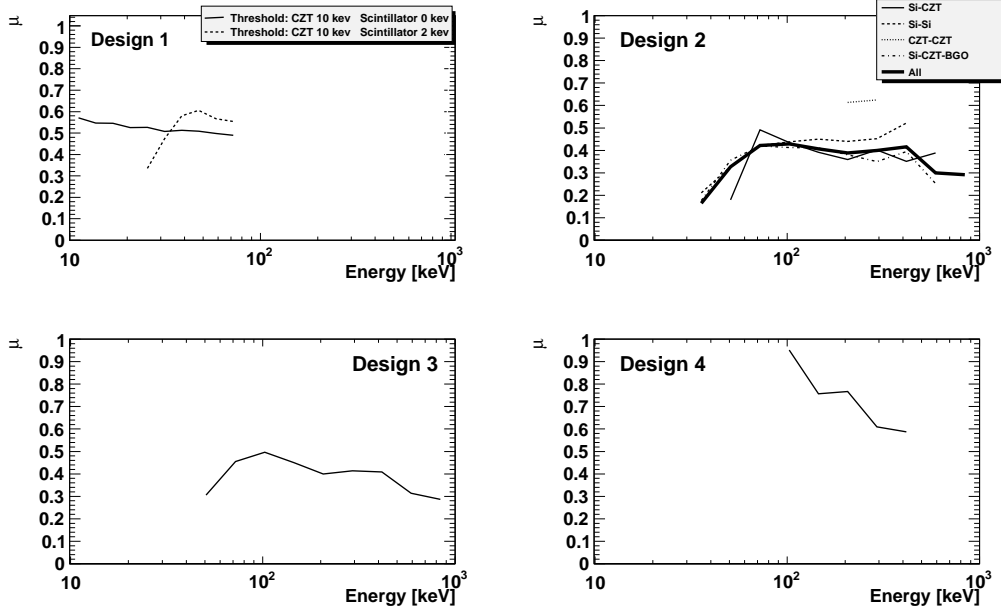


Figure 14: Modulation factors as function of energy for the four polarimeters. For Design 1 the modulation factors are shown for two trigger conditions. For Design 2 the modulation factors are shown when summing the ϕ -distributions over all event types (solid line) and for individual event types (other line styles, see legend).

large mass of the detectors of Designs 2-4 unavoidably scatters high-energy photons and particles and leads to a comparatively high background.

We derived order of magnitude estimates of the expected background rate for Design 1 and for Designs 2-4. The results can be used to get a rough estimate for which detector configurations and source strengths the background may indeed be negligible. Our background estimates for Design 1 assume three identical mirror/polarimeter assemblies. Each mirror assembly has an effective mirror area of 533 cm^2 , a maximum mirror diameter of 40 cm, and a focal length of 10 m. Each of the three mirror assemblies could be similar to the two mirror assemblies used for the NuSTAR mission [124]. The three mirror assemblies focus the X-rays onto three identical polarimeters of Design 1. Assuming an aperture of 4° diameter (similar to the one used of NuSTAR), we estimate a very low 10-80 keV CXB aperture flux count rate. The count rate from CXB photons being focussed by the mirrors onto the scattering slab is somewhat larger but still below 1/1000 of

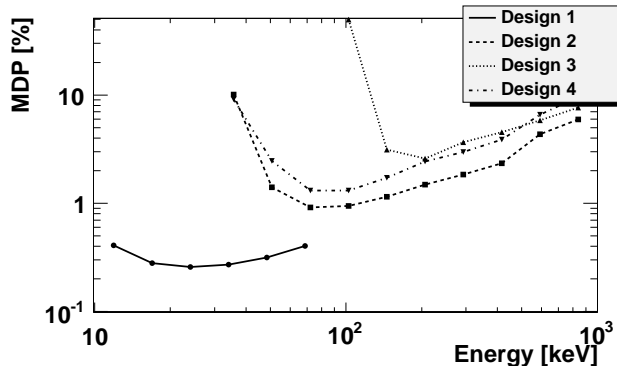


Figure 15: Differential MDPs of the four polarimeters. The binning was chosen to have six statistically independent bins between 10 keV and 80 keV (Design 1) and ten statistically independent bins between 30 keV and 1 MeV (Designs 2-4). For all four designs the binning corresponds to a $\Delta \log_{10} E$ of 0.15 per energy bin. The lines between the data points are only shown to guide the eye.

the count rate produced by a 1 Crab source. The dominant background will probably be internal backgrounds and the shield leakage background. Using the 10 keV - 80 keV background estimate of $3 \times 10^{-4} \text{ s}^{-1} \text{ cm}^{-2} \text{ keV}^{-1}$ from the simulations of the NuSTAR experiment [124], we estimate that the high-background event sample (no scintillator coincidence required) will have a total background count rate corresponding to the rate of Compton scattered events from a 17 mCrab source. This estimate accounts for all the background events in 96 CZT detectors of the three identical polarimeters, and assumes a combination of active and passive shielding and the reduction of background events based on the reconstruction of the depths of the interactions, similar as used for NuSTAR. We conclude that the high-background event sample will be signal dominated for sources with fluxes exceeding ~ 20 mCrab. The low-background event sample (with a coincident trigger in the scintillator) will have a much lower background. Simulations are underway to determine this background rate.

For Designs 2-4 the CXB aperture background flux will be relatively low – if the detector assemblies are used with a narrow field of view collimator assembly. *ASTRO-H* will use a collimator with an aperture of $0.55^\circ \times 0.55^\circ$ at low energies (< 150 keV) and with an aperture of $10^\circ \times 10^\circ$ at high energies

(>150 keV) [16]. For the smaller aperture, the 50-150 keV CXB aperture flux corresponds to a flux of 0.6 mCrab. For the larger aperture, the 150 keV-300 keV CXB aperture flux gives the same count rate as a source with a flux of 108 mCrab. The dominant background of designs 2-4 will probably come from internal backgrounds and shield leakage. A background rate of $3 \times 10^{-4} \text{ s}^{-1} \text{ cm}^{-2} \text{ keV}^{-1}$ will produce the same rate of 50-150 keV (150-300 keV) events as a source with a flux of 425 mCrab (3 Crab). Our estimate of the background count rate is motivated by the simulation results for NuSTAR and by our own simulations of detector configurations similar to Design 4. Takahashi et al. (2008) [16] estimate a two orders of magnitude lower internal background rate per unit area for the Si and CdTe detector assembly of the *ASTRO-H* soft gamma-ray telescope - but the estimate still needs experimental verification. From the discussion it is clear that if such extremely low background rates cannot be achieved in orbit, then only bright galactic sources can outshine the background. If the detector assemblies of Designs 2-4 are used in wide field of view instruments, then the CXB aperture flux becomes the dominant background. Assuming a 1 sr field of view, the 50-150 keV and 150-300 keV aperture fluxes correspond to source strengths of 6.1 Crab and 4.2 Crab, respectively. In this case, only bright GRBs can outshine the background.

The four detector assemblies differ not only in the accessible energy ranges and the achieved sensitivities. The solid state experiments (Designs 1, 2, and 4) exhibit a much better spectroscopic performance than the scintillator-only experiment (Design 3). For thick CZT detectors full width half maximum energy resolutions of 2.5 keV at 59 keV, 2.7 keV at 122 keV and 4 keV at 662 keV have been reported [150]. The Si strip detectors operated at -30° achieve ~ 1 keV energy resolutions. The narrow FoV polarimeter would achieve a good effective energy resolution even though the energy resolution of the scintillator is poor. The reason is that < 80 keV photons lose only a small fraction of their initial energy in Compton interactions (compare Fig. 4). The BGO scintillators used in Design 3 have a much poorer energy resolution than the CZT detectors used in Designs 1, 2 and 4, i.e. about ~ 50 keV FWHM at energies of a few 100 keV [133]. When used with a coded mask, the solid state polarimeters (Designs 2 and 4) achieve better angular resolutions than the scintillator polarimeter (Design 3) as the best possible angular resolution scales linearly with the CZT pixel pitch (0.6 mm and 2.5 mm), the Si strip pitch (1.4 mm), and the scintillator slab pitch (6.35 mm). It should be noted that this section compared instruments to each other with different degrees of complexity, different sizes, masses, and costs.

3.5. Calibration Issues

Proper on-ground and in-orbit calibration of the experiments will be crucial for achieving performances which are limited by the statistics of the detected Compton scattered events. We will address several issues in the following: the calibration of the detector response to photons, systematic uncertainties owing to background events, and other technical challenges.

One topic of major importance is the calibration of the energy thresholds of individual detector elements. Depending on the employed analysis method, the energy threshold may depend on the hardware trigger threshold, on the analysis cuts used to select valid events, or on both. A detailed analysis should account for the fact that the threshold behavior of the j^{th} detector element is given by the detection probability $p_j(E)$ as function of the energy E deposited in the detector element. Whereas $p_j(E)$ is almost a step function for detectors with excellent energy resolutions (e.g. Si and CZT detectors), it is a slowly varying function of energy for detectors with poorer energy resolutions (e.g. CsI, and much more so for plastic scintillators). As most sources have steeply falling energy spectra $dN/dE \propto E^{-\Gamma}$ with $\Gamma \approx 2 - 4$, an uncertainty of the energy threshold by a factor of $\Delta E/E$ will result in a count rate uncertainty by $\approx (\Gamma - 1)\Delta E/E$. If one is interested in measurements of the polarization fraction and the polarization direction in multiple energy bins, then one needs to know the probability $q_{j,k}(E)$ that an event depositing the energy E in the j^{th} detector element will be recorded and will be reconstructed in the k^{th} energy bin. Inferring the functions $q_{j,k}(E)$ will usually require a good calibration of the energy scale (absolute offsets and linearity) and the energy resolution. The functions $p_j(E)$ and $q_{j,k}(E)$ can be determined from detailed calibration measurements with a series of radioactive sources of known activity.

For all the designs, the energy threshold of the Compton scatterer is of special interest as it determines the lower energy threshold for detecting Compton events. For Design 1 one can use a single radioactive source with a strong emission line at an energy $E_\gamma \approx 100$ keV to make a precision measurement of $p_j(E)$ of the scintillator rod at energies $E \ll E_\gamma$ by Compton scattering photons off the scintillator rod and by detecting the scattered photons with CZT detectors positioned at different scattering angles. The Compton formula Equ. (12) can be used to infer E (or a range of possible E -values) when the scattering angle and the energy deposited in the CZT detector are known. The comparison of the expected and observed rates of Compton events can be used to infer $p_j(E)$. In practice, the method is a bit

more complicated and less unambiguous owing to the fact that the suitable radioactive sources (i.e. ^{57}Co) have multiple emission lines. A similar procedure can be used for measuring $p_j(E)$ for the low-Z plastic scintillators of Designs 3.

The science payload has to include suitable calibration sources to make sure that the ground calibration remains valid during the flight of the experiments. One needs to be careful to avoid aging scintillators (oxidation of hygroscopic materials) and variations of the detector gains owing to temperature and/or magnetic field variations during the flight. Although radiation damage is a concern, the effect seems to be rather small for recent missions (e.g. for the Swift BAT and for Fermi).

In addition to characterizing the energy response of the detectors, the active volume of each detector element V_j has to be measured to allow for an appropriate flat-fielding of the experiment. In CZT detectors for example, V_j is usually smaller for pixels close to the edges of a detector owing to the electric field line geometry inside the detector. In addition, impurities like Te-precipitates can affect V_j . Some care has to be taken to disentangle rate variations stemming from variable energy thresholds (resulting in different numbers of detected Compton continuum events) from rate variations stemming from partially inactive detector volumes. When integrating the detectors into the experiment, the detectors should be distributed as to minimize systematic biases.

The response of the entire instrument to X-rays and gamma-rays should be tested with polarized and unpolarized sources located at different locations relative to the experiment.

The backgrounds on high-altitude balloon flights and on satellite orbits is the next concern. As for all X-ray experiments a proper background subtraction is crucial for the proper determination of fluxes and energy spectra. It is highly desirable to have experiments which acquire simultaneous ON (source) and OFF (background) data. Only the simultaneous acquisition of ON and OFF source data enable strictly differential measurements and guarantee that time dependent backgrounds impact both data sets at the same time. Experiments which take ON data only, are notoriously difficult to calibrate in-orbit. If Designs 2-3 are used in coded aperture instruments, ON and OFF data are taken at the same time, allowing for proper background subtraction. A possibility to enable simultaneous ON and OFF measurements for Design 1 would be the addition of a second scintillator with a long decay time surrounding the scattering rod. Pulse shape discrimination could be

used to distinguish between hits in the central scattering rod and hits in the surrounding scintillator. An alternative could be the addition of a pixelated or cross-strip Si detector surrounding the scattering rod close to the focal plane of the mirror assembly. The Si detector could be used to flag events from the OFF region and to obtain imaging spectropolarimetric information of extended sources.

Another concern are spatial gradients of the background intensity (or the detector response) which might lead to background counts producing an azimuthal modulation of the count rate. Detailed Monte Carlo simulation of the entire satellite need to be carried through to estimate the magnitude of such effects and to modify the design in the case that the effect is strong. Data taken in-orbit can be used to search for such effects using observations of presumably unpolarized sources (symmetric galaxy clusters), empty regions in the sky, or repeated observations of one and the same sources at different parts of an orbit, or with different background conditions.

Compton telescopes are particularly sensitive to cross talk between detector elements producing artificial coincidences. Optical cross talk and MAPMT cross talk is an issue for Design 3; charge sharing, weighting potential, and electronic cross-talk are issues of Design 4 where hits in adjacent pixels can be mis-classified as Compton events. These effects can be studied by testing the polarimeter over the entire relevant energy range in the laboratory.

The discussion in this section shows that the calibration of an X-ray polarimeter is a major issue. The calibration of experiments with good or excellent energy resolution and with physically separated low-Z scatterers and high-Z absorbers (Designs 1 and 2) is probably more straight forward than the calibration of polarimeters with very poor energy resolution and/or where multiple interactions are detected in one and the same detector (Designs 3 and 4).

4. Summary and Discussion

Hard X-ray observations have to cope with the steep energy spectra of most astrophysical sources, and thus with lower photon fluxes than those in the soft X-ray band. However, hard X-ray polarimetry is an exciting upcoming field owing to several facts:

- Several phenomena can *only* be observed at hard X-rays. Examples are the measurement of the high-energy end of the thermal emission

from BBHs coming from the immediate surrounding of the black holes, observations of polarized cyclotron lines of magnetars, and the measurement of the polarization near the high-energy cutoffs of magnetars owing to the effect of photon splitting.

- Almost all science topics that can be addressed with soft X-ray polarimetry benefit greatly from *simultaneous soft and hard X-ray spectropolarimetric observations*. The broadband energy dependence of the polarization degree and direction is crucial to verify that the models used to explain the soft X-ray polarization results are actually correct. In several cases combined soft and hard X-ray polarimetry observations are required to determine the model parameters that affect the interpretation of the results obtained in the two bands. A prominent example is the study of BBH systems: the combined soft and hard X-ray observations are needed to constrain the parameters describing the black hole, the accretion disk, and the corona.
- In some sources the polarization degrees at higher energies are expected to be higher than at lower energies owing to the more compact emission regions of hard X-rays. For some sources the effect may make it easier to measure the hard X-ray polarization than the soft X-ray polarization.
- Hard X-rays allow us to study heavily obscured sources with column densities exceeding 10^{24} cm^{-2} .
- For very hard sources (i.e. hard GRBs) hard X-ray observations achieve similar MDPs as soft X-ray observations as the photon number only depends logarithmically on the low energy threshold.

Table 2 shows the science topics that can be addressed with the different instrument designs. The table accounts for the different energy ranges of the four polarimeters and for their different field of views (Design 1: narrow field of view, Designs 2-4: possibly wide field of views). An estimate of the actual numbers of detected sources requires careful optimization of the shielding concept and is outside the scope of this paper.

In the light of the results shown in the table three *GEMS* and *ASTRO-H* follow-up missions are attractive. The first mission is a narrow FoV broadband X-ray polarimetry mission with good sensitivity in the 0.1 keV-2 keV energy regime, an order of magnitude improved sensitivity and/or imaging

	Design 1	Design 2	Design 3	Design 4
BBH thermal disk emission	✓	-	-	-
BBH coronal emission	✓	✓	✓	✓
X-ray/ γ -ray pulsars	-	✓	✓	✓
NS cyclotron lines	✓	-	-	-
NS vacuum birefringence	✓	-	-	-
Magnetar X-ray tails	✓	✓	✓	✓
Magnetar photon splitting	-	✓	✓	✓
AGN coronae	\sim	-	-	-
Blazar jets	✓	✓	✓	✓
GRB jets	\sim^a	✓	✓	✓
Solar Flares	\sim^b	✓	✓	✓
Stellar Flares	-	-	-	-
LIV	✓	✓	✓	✓

^a Requires alert by another instrument.

^b A narrow field of view instrument would be unlikely to detect exceptionally strong solar flares without alerts from other instruments.

Table 2: Science topics that can be addresses with the four different instrument designs.

spectropolarimetric capabilities in the 2 keV-10 keV energy band, and with spectropolarimetric coverage up to 80 keV. The second mission is a wide FoV observatory for spectropolarimetric studies of GRBs and flaring galactic sources, e.g. similar to EXIST, a large HX-POL, or POET. There is a niche for a large area detector assembly (similar to HX-POL, GRAPE) used with a pencil beam collimator to measure the >80 keV polarization properties of galactic sources, e.g. BBHs and the various flavors of neutron stars.

The Washington University hard X-ray group is presently assembling a polarimeter called *X-Calibur* which adopts Design 1. We will report on detailed calibration measurements and on comparisons of simulated and experimentally measured data in a forthcoming paper. Pending approval by NASA, the polarimeter will be flown on a one-day balloon flight in the focal plane of an *InFOCUS* mirror assembly [125] with $\sim 40\text{cm}^2$ detection area in spring 2012 and on subsequent longer balloon flights from Australia. In a collaboration with the Naval Research Laboratory (E. Wulff et al.), the group is also testing prototypes of the *HX-POL* Si-CZT polarimeter (Design 2).

Acknowledgements: The authors thank Martin Israel, Jonathan Katz (both Washington Univ. in St. Louis), Paolo Coppi (Yale), and J. Schnittman (Goddard Space Flight Center) for reading the manuscript carefully and for very valuable suggestions. Insightful comments by an anonymous referee helped to strengthen the paper substantially. HK acknowledges NASA for support from the APRA program under the grant NNX10AJ56G and support from the high-energy physics division of the DOE. The Washington University group is grateful for discretionary funding of the *X-Calibur* polarimeter by the McDonnell Center for the Space Sciences.

References

- [1] Giacconi, R., Branduardi, G., Briel, U., et al. 1979, *ApJ.*, 230, 540
- [2] Trümper, J. 1983, *Adv. Space. Res.*, 2, No. 4, 241
- [3] Weisskopf, M. C. et al. 2002, *Publ. Astron. Soc. Pacif.* 114, 1
- [4] Strüder, L., Briel, U., Dennerl, K., et al. 2001, *A&A*, 265, L18
- [5] Jahoda, K., Swank, J., Giles, A.B., et al. 1996, *Proc. SPIE*, 2808, 59
- [6] Mitsuda, K. et al. 2007, *PASJ*, 59, S9
- [7] Novick, R. 1975, *Space Sci. Rev.*, 18, 389
- [8] Weisskopf, M. C., Silver, E. H., Kestenbaum, H. L., Long, K. S., Novick, R. *ApJL*, 220, L117
- [9] Silver, E. H., Weisskopf, M. C., Kestenbaum, H. L., Long, K. S., Novick, R., Wolff, R. S. 1979, *ApJ*, 232, 248
- [10] Hughes, J. P., Long, K. S., Novick, R. 1984, *ApJ*, 280 255
- [11] Dean, A. J., Clark, D. J., Stephen, J. B., et al. 2008, *Science*, 321, 1183
- [12] Forot, M., Laurent, P., Grenier, I. A., Gouïffs, C., Lebrun, F. 2008, *ApJL*, L688, 29
- [13] Hill, J. E., Barthelmy, S., Black, J. K., et al. 2007, *SPIE*, vol. 6686, 29, pp. 66860Y-66860Y-12, Sept. 2007.

- [14] Costa, E., Bellazzini, R., Bregeon, J., et al. 2007, *Proc. SPIE*, vol. 7011, pp. 15, arXiv0810.2700C.
- [15] Swank, J., et al. <http://heasarc.gsfc.nasa.gov/docs/gems/>
- [16] Takahashi, T., Kelley, R., Mitsuda, K., et al., “The NeXT Mission”, *Space Telescopes and Instrumentation 2008: Ultraviolet to Gamma Ray*. Edited by Turner, Martin J. L.; Flanagan, Kathryn A. Proceedings of the SPIE, Volume 7011, pp. 70110O-70110O-14, 2008.
- [17] Lei, F., Dean, A. J., Hills, G. L. 1997, *Space Sci. Rev.*, 82, 309
- [18] Weisskopf, M. C., Elsner, R. F., Hanna, D., Kaspi, V. M., O’Dell, S. L., Pavlov, G. G., Ramsey, B. D. 2006, “X-Ray Polarimetry and Its Potential Use for Understanding Neutron Stars”, in *Neutron Stars and Pulsars, Astrophysics and Space Science Library, Volume 357*. ISBN 978-3-540-76964-4. Springer Berlin Heidelberg, p. 589 2009 [astro-ph/0611483]
- [19] Bellazzini, R., Costa, E., Matt, G., Tagliaferri, G. (eds.), “X-ray Polarimetry: A New Window in Astrophysics”, *Cambridge Contemporary Astrophysics* (2010)
- [20] Remillard, R. A., McClintock, J. E. 2006, *ARA&A*, 44, 49
- [21] Chandrasekhar, S. 1960, *Radiative Transfer* (New York: Dover)
- [22] Angel, J. R. P. 1969, *ApJ*, 158, 219
- [23] Sunyaev, R. A., Titarchuk, L. G. 1985, *A&A*, 143, 374
- [24] Stark, R. F., Connors, P. A. 1977, *Nature*, 266, 429
- [25] Connors, P. A., Piran, T., Stark, R. F. 1980, *ApJ*, 235, 224
- [26] Connors, P. A., Stark, R. F. 1980, *Nature*, 269, 128
- [27] Dovciak, M., Karas, V., Matt, G. 2004, *MNRAS*, 355, 1005
- [28] Dovciak, M., Muleri, F., Goodmann, R. W., Karas, V., Matt, G. 2008, *MNRAS*, 391, 32
- [29] Agol, E., Krolik, J. H. 2000, *ApJ*, 528, 161

- [30] Schnittman, J. D., Krolik, J. H. 2009, ApJ, 701, 1175
- [31] Schnittman, J. D., Krolik, J. H. 2010, ApJ, 712, 908
- [32] Abdo, A. A., Ackerman, M., Ajello, M., et al. 2010, ApJS, 187, 460
- [33] Muslimov, A. G. & A. K. Harding 2003, Astrophysical Journal, 588, 430
- [34] Romani, R. W. 1996, Astrophysical Journal, 470, 469
- [35] Romani, R. W., & Watters, K. P. 2010, Astrophysical Journal, 714, 810
- [36] Pierbattista, M., Grenier, I., Harding, A., & Gonthier, P. 2010, Proc. of the 2009 Fermi Symposium, eConf C091122, [arXiv:1002.0324]
- [37] Coburn, W., Heindl, W. A., Rothschild, R. E., Gruber, D. E., Kreykenbohm, I., Wilms, J., Kretschmar, P., & Staubert, R. 2002, ApJ, 580, 394
- [38] Heindl, W. A., Rothschild, R. E., Coburn, W., Staubert, R., Wilms, J., Kreykenbohm, I., Kretschmar, P. 2004, AIP 714, 323
- [39] Ghosh, P. 2007, “Rotation and Accretion Powered Pulsars”, World Scientific, Hackensack, New Jersey, pp. 472
- [40] Nakajima, M., Mihara, T., Makishima, K., Enoto, T., Terada, Y., Nakazawa, K. 2008, “The X-ray Universe 2008”, Symposium in Granada, Spain, online at http://xmm.esac.esa.int/external/xmm_science/workshops/2008symposium/
- [41] Meszaros, P., Novick, R., Szentgyorgyi, A., Chanan, G. A., Weisskopf, M. C. 1988, ApJ, 324, 1056
- [42] Heindl, W. A., Coburn, W., Gruber, D. E., Pelling, M. R., Rothschild, R. E., Wilms, J., Pottschmidt, K., Staubert, R. 2000, AIP 510, 173
- [43] Lai, D., Ho, W. C. 2003, Phys. Rev. Lett., 91, 1101
- [44] Lai, D., Ho, W. C. 2003, ApJ, 588,962
- [45] Lutovinov, A. A., Tsygankov, S. S. 2009, Astronomy Letters, 35, 433
- [46] van Adelsberg, M., Lai, D., 2006, MNRAS, 373, 1495

- [47] Esposito, P., et al. 2007, A&A, 476, 321
- [48] Mereghetti, S., Götz, D., von Kienlin, A., Rau, A., Lichti, G., Weidenspointner, G., & Jean, P. 2005, ApJL, 624, L105
- [49] Perna, R., Heyl, J. S., Hernquist, L. E., et al. 2001, Astrophysical Journal, 557, 18
- [50] Lyutikov, M. & Gavriil, F. P. 2006, Monthly Notices of the Royal Astronomical Society, 368, 690
- [51] Nobili, L., Turolla, R. & Zane, S. 2008, Monthly Notices of the Royal Astronomical Society, 386, 1527
- [52] Kuiper, L., Hermsen, W., den Hartog, P. R., et al. 2006, Astrophysical Journal, 645, 556
- [53] Götz, D., Mereghetti, S., Tiengo, A., et al. 2006, A&A, 449, L31
- [54] den Hartog, P. R., Kuiper, L., Hermsen, W., et al. 2008, A&A, 489, 245
- [55] Baring, M. G. & Harding A. K. 2007, Ap&SS, 308, 109
- [56] Baring, M. G. 2008, in *Proc. CASYS '07 Conference "Computing Anticipatory Systems,"* ed. D. M. Dubois (AIP Conf. Proc. 1051, New York), p. 53. [[astro-ph/0804.0832](https://arxiv.org/abs/astro-ph/0804.0832)]
- [57] Thompson, C. & Duncan, R. C. 1996, Astrophysical Journal, 473, 332
- [58] Nandra, K., Pounds, K. A., Stewart, G. C., George, I. M., Hayashida, K., Makino, F., & Ohashi, T. 1991, MNRAS, 248, 760
- [59] Mushotzky, R. F., Done, C., Pounds, K. A. 1993, ARA&A, 31, 717
- [60] Haardt, F., Maraschi, L. 1993, ApJ, 413, 507
- [61] Reynolds, C. S., Nowak, M. A. 2003, Phys. Rep., 377, 389
- [62] Piro L., Nicastro F., Feroci M. et al. 1998, Nucl. Phys. B, 69/1-3, 481
- [63] Piro, L., de Rosa, A., Dadina, M., et al. 2000, Advances in Space Research, 25, 453

- [64] Poutanen, Y. 1994, *ApJS*, 92, 607
- [65] Celotti, A, Matt, G. 1994, *MNRAS*, 268, 451
- [66] McNamara, A. L., et al. 2009, <http://arxiv.org/abs/0902.1562>.
- [67] Angel, J. R. P., Stockman, H. S. 1980, *ARAA*, 8, 321
- [68] Scarpa, R., Falomo, R. 1997, *A&A*, 325, 109
- [69] Marscher, A. P., Jorstad, S. G., D’Arcangelo, F. D., et al. 2008, *Nature*, 452, 966
- [70] Abdo, A. A., Ackermann, M., Ajello, M., et al. 2010a, *Nature* 463, 919
- [71] Woosley, S. E. 1993, *ApJ*, 405, 273
- [72] Paczynski, B. 1998, *ApJ*, 494, L45
- [73] Gehrels, N., et al. 2005, *Nature*, 437, 851
- [74] Rees, M. J., Meszaros, P. 1994, *ApJ*, 430, L93
- [75] McKinney, J. C. 2006, *MNRAS*, 368, 1561
- [76] Coburn, W., Boggs, S. E. 2003, *Nature*, 423, 415
- [77] Rutledge, R. E., & Fox, D. B. 2004, *MNRAS*, 350, 1288
- [78] Kalemci, E., Boggs, S. E., Kouveliotou, C., Finger, M., & Baring, M. G. 2007, *ApJS*, 169, 75
- [79] McGlynn, S., et al. 2007, *A&A*, 466, 895
- [80] Götz, D., Laurent, P., Lebrun, F., Daigne, F., & Bošnjak, Ž. 2009, *ApJL*, 695, L208
- [81] Granot, J., Knigl, A. 2003, *ApJL*, 594, 83
- [82] Eichler, D., Levinson, A. 2003, *ApJL*, 596, 147
- [83] Lyutikov, M., Pariev, V. I., Blandford, R. D. 2003, *ApJ*, 597, 998
- [84] Waxman, E. 2003, *Nature*, 423, 388

- [85] Rossi, E. M., Lazzati, D., Salmonson, J. D., Ghisellini, G. 2004, MNRAS, 354, 86
- [86] Barthelmy, S. D., Barbier, L. M., Cummings, J. R., et al. 2005, SSR, 120, 143
- [87] Ajello, M., Greiner, J., Sato, G., et al. 2008, ApJ, 689, 666
- [88] O'Brien, P. T., Willingale, R., Osborne, J. 2006, ApJ, 647, 12130
- [89] Sakamoto, T., Barthelmy, S. D., Barbier, L., et al. 2008, ApJS, 175, 179
- [90] Lin, R. P., Hudson, H. S. 1976, Sol. Phys., 50, 153
- [91] Korchak, A. A. 1967, Soviet Phys. Dokl., 12, 192
- [92] Elwert, G. 1968, in IAU Symp. 35, Structure and Development of Solar Active Regions, ed. K. O. Kiepenheuer (Dordrecht: Reidel), 444
- [93] Emslie, A. G., Bradsher, H. L., McConnell, M. L. 2008, ApJ, 674, 570
- [94] Bai, T., Ramaty, R. 1978, ApJ, 219, 705
- [95] Leach, J., Petrosian, V. 1983, ApJ, 269, 715
- [96] Chanan, G., Emslie, A. G., Novick, R. 1988, Sol. Phys. 1988, 118, 309
- [97] Bogomolov, A. V., Denisov, Y. I., Kuznetsov, S. N., et al. 2003, Solar System Research, 37, 112
- [98] Boggs, S. E., Coburn, W., Kalemci, E. 2006, ApJ, 638, 1129
- [99] Suarez-Garcia, E., Hajdas, W., Wigger, C., Arzner, K., Güdel, M., Zehnder, A., & Grigis, P. 2006, Sol. Phys., 239, 149
- [100] Zhitnik, I. A., Logachev, Y. I., Bogomolov, A. V., et al. 2006, Solar System Research, 40, 93
- [101] Crosby, N. B., Aschwanden, M. J., Dennis, B. R. 1993, Sol. Phys., 143, 275

- [102] Franciosini, E., Pallavicini, R., Bastian, T., Chiuderi-Drago, F., Randich, S., Tagliaferri, G., Massi, M., Neidhöfer, J. 1999, 11th Cambridge Workshop on Cool Stars, Stellar Systems, and the Sun, eds. R. J. García López, R. Rebolo, M. R. Zapaterio Osorio (San Francisco: ASP), 930
- [103] Güdel, M. 2004, *Astronomy and Astrophysics Review*, 12, 71
- [104] Mattingly, D. 2005, *Living Reviews in Relativity*, 8, 5, <http://relativity.livingreviews.org/Articles/lrr-2005-5/>
- [105] Jacobson, T., Liberati, S., Mattingly, D. 2006, *Annals of Physics*, 321, 150
- [106] Will, C., *Living Reviews in Relativity*, 9, 3, <http://relativity.livingreviews.org/Articles/lrr-2006-3/>
- [107] Liberati, S., & Maccione, L. 2009, *Annual Review of Nuclear and Particle Science*, 59, 245
- [108] Colladay, D., Kostelecký, V. A., 1997, *Phys. Rev. D* 55, 6760
- [109] Colladay, D., Kostelecký, V. A., 1997, *Phys. Rev. D* 58, 116002
- [110] Amelino-Camelia, G., Ellis, J. R., Mavromatos, N. E., Nanopoulos, D. V., and Sarkar, S. 1998, *Nature* 393, 763
- [111] Abdo, A. A., Ackermann, M., Ajello, M., et al. 2009, *Nature*, 462, 331
- [112] Aharonian, F., Akhperjanian, A. G., Barres de Almeida, U., et al. 2008, *Phys. Rev. Lett.*, 101q0402A
- [113] Gambini, R., Pullin, J. 1999, *Phys. Rev. D* 59, 124021
- [114] Fan, Y. Z., Wei, D. M., Xu, D. 2007, *MNRAS*, 376, 1857
- [115] Kostelecký, V. A., Mewes, M. 2009, *Phys. Rev. D.*, 80a5020K
- [116] Berger, M. J., Hubbell, J. H., Seltzer, S. M., Chang, J., Coursey, J. S., Sukumar, R., Zuck, D. S. 2010, “XCOM: Photon Cross Sections Database”, <http://www.nist.gov/physlab/data/xcom/index.cfm>
- [117] Evans, R. D. 1955, “The atomic nucleus”, New York: McGraw-Hill

- [118] McConnell, M. L., Ryan, J. M., Smith, D. M., Emslie, A. G., Fivian, M., Hurford, G. J., Lin, R. P., “RHESSI Studies of Solar Flare Hard X-Ray Polarization”, *Bulletin of the American Astronomical Society*, Vol. 36, p. 668, 2004.
- [119] Mizuno, T., Kamae, T., Ng, J., et al. 2005, *NIMA*, 540, 158
- [120] Michel, T., Durst, J. 2008, *NIMA*, 594, 188
- [121] Vadawale, S. V., Paul, B., Pendharkar, J., & Naik, S. 2010, *NIMA*, 618, 182
- [122] Ramsey, B. D., Alexander, C. D., Apple, J. A., et al. 2002, *ApJ*, 568, 432
- [123] Harrison, F. A., Christensen, F. E., Craig, W., et al. 2005, *Experimental Astronomy*, 20, 131
- [124] Harrison, F. A., Boggs, S., Christensen, F., et al. 2010, *SPIE* 7732, 21
- [125] Ogasaka, Y., Tueller, J., Yamashita, K., et al. 2005, *SPIE*, 5900, 217
- [126] He, Z., Knoll, G. F., Wehe, D. K., et al. 1996, *NIMA*, 380, 228
- [127] He, Z., Knoll, G. F., Wehe, D. K., Miyamoto, J. 1997, *NIMA*, 388, 180
- [128] Krawczynski, H., Jung, I., Perkins, J., Burger, A., Groza, M. 2004, *Proc. SPIE*, 5540, 1
- [129] Krawczynski, H., Garson III, A., Martin, J., Beilicke, M., Grindlay, J., Hong, J. S., Skinner, G. K., Sturmer, S., for the EXIST team, Procs. ”Polarimetry days in Rome: Crab status, theory and prospects”, Rome, Italy, 16-17 October 2008, *Proceedings of Science*, http://pos.sissa.it/archive/conferences/078/026/CRAB2008_026.pdf
- [130] Xu, D., He, Z. 2006, *IEEE Trans. on Nucl. Sci.*, 53, 2787
- [131] McConnell, M. L., Angelini, L., Baring, M. G., et al. 2009a, *AIP Conf. Proc.*, 1133, 64
- [132] McConnell, M. L., Bancroft, C., Bloser, P. F., Connor, T., Legere, J., Ryan, J. M. 2009b, *SPIE*, 7435, 13

- [133] Bloser, P. F., Legere, J. S., McConnell, M. L., Macri, J. R., Bancroft, C. M., Connor, T. P., Ryan, J. M. 2009, NIMA, 600, 424
- [134] Krawczynski, H., Garson, A. III, Martin, J., et al. 2009, IEEE Trans. on Nucl. Sci., 56, 3607
- [135] Grindlay, J., and the EXIST Team, AIP 1133, 18 [arXiv:0904.2210]
- [136] Chen, C. M. H., Cook, W. R., Harrison, F. A., Lin, J. Y. Y., Mao, P. H., and Schindler, S. M. 2004, SPIE, 5198, 9
- [137] Hong, J. S., Grindlay, J., Allen, B., Skinner, G. K., Ubertini, P., Natalucci, L. 2009, and the EXIST team, Procs. "The Extreme sky: Sampling the Universe above 10 keV - extremesky", 2009 Otranto (Lecce) Italy October 13-17, 2009 Proceedings of Science, http://pos.sissa.it//archive/conferences//096/093/extremesky2009_093.pdf
- [138] Kim, J. C., Anderson, S. E., Kaye, W., Kaye, S. J., Zhu, Y., Zhang, F., He, Z. 2009, "Study on effect of charge sharing events in common-grid pixelated CdZnTe detectors", Nuclear Science Symposium Conference Record (NSS/MIC), 2009 IEEE , pp.1640, doi: 10.1109/NSS-MIC.2009.5402243
- [139] Zhang, F. 2005, "Events reconstruction in 3-D position sensitive CdZnTe gamma-ray spectrometers", Ph. D. Thesis, University of Michigan
- [140] Zhang, F., He, Z., Knoll, G. F., Wehe, D. K., Berry, J. E. 2005, IEEE Trans. on Nucl. Sci., 52, 2009
- [141] Agostinelli, S., Allison, J., Amako, K., et al. 2003, NIMA, 506, 250
- [142] Tueller, J., Baumgartner, W. H., Markwardt, C. B., et al. 2010, ApJS, 186, 378
- [143] Vinokur, M. 1965, Annales d'Astrophysique, 28, 412
- [144] Jenkins, G. M., Watts, D. G. 1968, "Spectral Analysis and Its Applications" (Holden-Day, San Francisco)
- [145] Depaola, G. O. 2003, NIMA, 512, 619

- [146] Kippen, R. M. 2004, *New Astron. Rev.*, 48, 221
- [147] McConnell, M. L., Kippen, R. M. 2004, *Bulletin of the American Astronomical Society*, 36, 1206
[http://public.lanl.gov/mkippen/actsim/papers/GLEPS_Poster_HEAD2004.pdf]
- [148] Legere, J., Blosier, P. L., Macri, J. R., McConnell, M. L., Narita, T., Ryan, J. M. 2005, *Proc. SPIE*, 5898, 413
- [149] Blosier, P. F., Legere, J. S., Macri, J. R., McConnell, M. L., Narita, T., Ryan, J. M. 2006, *Chin. J. of Astronomy and Astrophysics Supp.*, 6, 010000
- [150] Li, Q., Beilicke, M., Lee, K., et al. 2010, submitted to *Astroparticle Physics*